

The ATLAS^{3D} project – III. A census of the stellar angular momentum within the effective radius of early-type galaxies: unveiling the distribution of fast and slow rotators

Eric Emsellem,^{1,2*} Michele Cappellari,³ Davor Krajnović,¹ Katherine Alatalo,⁴ Leo Blitz,⁴ Maxime Bois,^{1,2} Frédéric Bournaud,⁵ Martin Bureau,³ Roger L. Davies,³ Timothy A. Davis,³ P. T. de Zeeuw,^{1,6} Sadegh Khochfar,⁷ Harald Kuntschner,⁸ Pierre-Yves Lablanche,² Richard M. McDermid,⁹ Raffaella Morganti,^{10,11} Thorsten Naab,¹² Tom Oosterloo,^{10,11} Marc Sarzi,¹³ Nicholas Scott,³ Paolo Serra,¹⁰ Glenn van de Ven,¹⁴ Anne-Marie Weijmans^{15†} and Lisa M. Young^{16‡}

¹European Southern Observatory, Karl-Schwarzschild-Str. 2, 85748 Garching, Germany

²Université Lyon 1, Observatoire de Lyon, Centre de Recherche Astrophysique de Lyon and Ecole Normale Supérieure de Lyon, 9 avenue Charles André, F-69230 Saint-Genis Laval, France

³Sub-department of Astrophysics, Department of Physics, University of Oxford, Denys Wilkinson Building, Keble Road, Oxford OX1 3RH

⁴Department of Astronomy, Campbell Hall, University of California, Berkeley, CA 94720, USA

⁵Laboratoire AIM Paris-Saclay, CEA/IRFU/Sap CNRS Université Paris Diderot, 91191 Gif-sur-Yvette Cedex, France

⁶Sterrewacht Leiden, Leiden University, Postbus 9513, 2300 RA Leiden, the Netherlands

⁷Max-Planck-Institut für extraterrestrische Physik, PO Box 1312, D-85478 Garching, Germany

⁸Space Telescope European Coordinating Facility, European Southern Observatory, Karl-Schwarzschild-Strasse 2, 85748 Garching, Germany

⁹Gemini Observatory, Northern Operations Center, 670 N. A'ohoku Place, Hilo, HI 96720, USA

¹⁰Netherlands Institute for Radio Astronomy (ASTRON), Postbus 2, 7990 AA Dwingeloo, the Netherlands

¹¹Kapteyn Astronomical Institute, University of Groningen, Postbus 800, 9700 AV Groningen, the Netherlands

¹²Max-Planck-Institut für Astrophysik, Karl-Schwarzschild-Str. 1, 85741 Garching, Germany

¹³Centre for Astrophysics Research, University of Hertfordshire, Hatfield, Herts AL1 9AB

¹⁴Max-Planck-Institut für Astronomie, Königstuhl 17, 69117 Heidelberg, Germany

¹⁵Dunlap Institute for Astronomy & Astrophysics, University of Toronto, 50 St George Street, Toronto, ON M5S 3H4, Canada

¹⁶Physics Department, New Mexico Institute of Mining and Technology, Socorro, NM 87801, USA

Accepted 2011 February 24. Received 2011 January 27; in original form 2010 November 3

ABSTRACT

We provide a **census** of the apparent stellar angular momentum within one effective radius of a volume-limited sample of 260 early-type galaxies (ETGs) in the nearby Universe, using the integral-field spectroscopy obtained in the course of the ATLAS^{3D} project. We **exploit** the λ_R parameter (previously used via a constant **threshold** value of 0.1) to characterize the existence of two families of ETGs: slow rotators which exhibit complex stellar velocity fields and often include stellar kinematically distinct cores, and fast rotators which have regular velocity fields. Our complete sample of 260 ETGs leads to a new **criterion to disentangle** fast and slow rotators which now includes a dependency on the apparent ellipticity ϵ . It separates the two classes significantly better than the previous prescription and better than a criterion based on V/σ : slow rotators and fast rotators have λ_R lower and larger than $k_{FS} \times \sqrt{\epsilon}$, respectively, where $k_{FS} = 0.31$ for measurements made within an effective radius R_e .

We show that the **vast majority** of ETGs are fast rotators: these have the regular stellar rotation, with **aligned** photometric and kinematic axes (Paper II of this series), include discs and often bars and represent 86 ± 2 per cent (224/260) of all ETGs in the volume-limited

*E-mail: eric.emsellem@eso.org

†Dunlap Fellow.

‡Adjunct Astronomer with the National Radio Astronomy Observatory.

ATLAS^{3D} sample. Fast rotators span the full range of apparent ellipticities from $\epsilon = 0$ to 0.85, and we suggest that they cover intrinsic ellipticities from about 0.35 to 0.85, the most flattened having morphologies consistent with spiral galaxies. Only a small fraction of ETGs are slow rotators representing 14 ± 2 per cent (36/260) of the ATLAS^{3D} sample of ETGs. Of all slow rotators, 11 per cent (4/36) exhibit two counter-rotating stellar disc-like components and are rather low-mass objects ($M_{\text{dyn}} < 10^{10.5} M_{\odot}$). All other slow rotators (32/36) appear relatively round on the sky ($\epsilon_e < 0.4$), tend to be massive ($M_{\text{dyn}} > 10^{10.5} M_{\odot}$), and often (17/32) exhibit kinematically distinct cores. Slow rotators dominate the high-mass end of ETGs in the ATLAS^{3D} sample, with only about one-fourth of galaxies with masses above $10^{11.5} M_{\odot}$ being fast rotators. We show that the a_4 parameter which quantifies the isophote's disciness or boxiness does not seem to be simply related to the observed kinematics, while our new criterion based on λ_R and ϵ is nearly independent of the viewing angles. We further demonstrate that the classification of ETGs into ellipticals and lenticulars is misleading. Slow and fast rotators tend to be classified as ellipticals and lenticulars, respectively, but the contamination is strong enough to affect results solely based on such a scheme: 20 per cent of all fast rotators are classified as ellipticals, and more importantly 66 per cent of all ellipticals in the ATLAS^{3D} sample are fast rotators.

Fast and slow rotators illustrate the variety of complex processes shaping galactic systems, such as secular evolution, disc instabilities, interaction and merging, gas accretion, stripping and harassment, forming a sequence from high to low (stellar) baryonic angular momentum. Massive slow rotators represent the extreme instances within the red sequence of galaxies which might have suffered from significant merging without being able to rebuild a fast-rotating component within one effective radius. We therefore argue for a shift in the paradigm for ETGs, where the vast majority of ETGs are galaxies consistent with nearly oblate systems (with or without bars) and where only a small fraction of them (less than 12 per cent) have central (mildly) triaxial structures.

Key words: galaxies: elliptical and lenticular, cD – galaxies: evolution – galaxies: formation – galaxies: kinematics and dynamics – galaxies: structure.

1 INTRODUCTION

Early-type galaxies (ETGs) lie at one end of the Hubble tuning fork, the schematic ordering of galaxy morphology classes established long ago (Hubble 1936; de Vaucouleurs et al. 1991), the late-type spirals being located at the other end of the diagram (excluding irregulars). Although the Hubble sequence is not thought to represent an evolutionary sequence, early-type systems are generally considered to be the output of violent and extreme processes mainly driven by interactions and mergers in a hierarchical Universe, in contrast to formation processes advocated for spiral galaxies.

At moderate to high redshifts, the difficulty to obtain detailed photometric and spectroscopic information of large numbers of systems often leads to gathering ETGs into a single class: ETGs are generally viewed as a single family of objects, separated from the line of spiral systems, and which can be studied at various redshifts (e.g. Bell et al. 2004; McIntosh et al. 2005; Kriek et al. 2008). There are nowadays various techniques to build samples of ETGs from large surveys, for example, the colour/spectroscopic information based on the fact that most galaxies in the red sequence are early types (see e.g. Bell et al. 2004, and references therein). This obviously includes the visual classification which, when applied at relatively lower redshift, can lead to a classification closer to the full-fledged schemes defined by Hubble or de Vaucouleurs (Fukugita et al. 2007).

For nearby samples of galaxies, ETGs are more commonly separated into two groups, namely the ellipticals (Es) and lenticulars

(S0s), the latter being a transition class to (or from) the spiral systems (Hubble 1936). This is the existing paradigm for ETGs, nicely illustrated by, for example, the work conducted by Bernardi et al. (2010) who studied a large set of galaxies extracted from the Sloan Digital Sky Survey. ETGs are mostly red-sequence objects, comprising Es and S0s, each class representing about half of such a magnitude-limited sample of ETGs. All together, Es and S0s represent a significant fraction (~ 40 per cent) of the total stellar mass density in the nearby Universe (Fukugita et al. 2007; Bernardi et al. 2010). Es are thought to be nearly pure spheroidal objects, sometimes with central discs, while S0s are disc galaxies with large bulges/spheroidal components. Es are on average rounder than S0s, with very few Es having ellipticities higher than 0.4, and dominate the high-mass range of ETGs.

This picture has been regularly and significantly updated specifically for galaxies in the nearby Universe for which we often have exquisite photometric and spectroscopic information (Bender, Saglia & Gerhard 1994; Gerhard et al. 1999; Rix, Carollo & Freeman 1999). An attempt to, for instance, further refine the elliptical E class into the boxy and discy systems was pursued by Kormendy & Bender (1996): the proposed classification recognizes the sequence of intrinsic flattening and shapes and tries to address the presence of discs (Rix & White 1990; Scorza & van den Bosch 1998; Naab & Burkert 2001) and the dynamical status of these galaxies via a photometric proxy (namely, a_4 , representing part of the deviation of isophotes from pure ellipses). This has been recently expanded in the context of the ‘light deficit/excess’

(Graham & Guzmán 2003; Graham 2004; Côté et al. 2006; Ferrarese et al. 2006; Kormendy et al. 2009) to examine whether or not different groups of Es **may be the key to link photometric properties with their formation and assembly scenarios** (Naab, Burkert & Hernquist 1999; Khochfar & Burkert 2005; Hopkins et al. 2009a,c; Kormendy et al. 2009). Nevertheless, ETGs continue to be divided into elliptical (spheroidal-like) and lenticular (disc-like) systems, the former exhibiting some mild triaxiality (usually associated with the anisotropy), while the latter are prone to typical disc perturbations, for example, bars.

There are many complications associated to these classification schemes due to, for example, inclination effects or the limitations of photometric measurements (Kormendy & Bender 1996; Cappellari et al. 2007, hereinafter C+07). It is hard to disentangle S0s from Es, which limits the conclusions from studies using these as prime ingredients. Emsellem et al. (2007, hereinafter E+07) have emphasized the fact that stellar kinematics contain critical information on the actual dynamical status of the galaxy. E+07 suggested that λ_R , a simple parameter which can be derived from the first two stellar velocity moments, can be used as a robust estimator of the apparent specific angular momentum (in stars) of galaxies (see also Jesseit et al. 2009).

Following this prescription, E+07 and C+07 have shown that ETGs can be classified into two broad families depending on their λ_R values: **(i) slow rotators (SRs) ($\lambda_R < 0.1$), which show little or no rotation, significant misalignments between the photometric and the kinematic axes, and contain kinematically decoupled components; and (ii) fast rotators (FRs) ($\lambda_R \geq 0.1$), which exhibit regular stellar velocity fields, consistent with the disc-like rotation (Krajnović et al. 2008) and sometimes bars.** These results were, however, based on a representative (but not complete) sample of 48 ETGs that is not a fair sample of the local Universe.

We are now in a position to re-examine these issues in light of the volume-limited ATLAS^{3D} survey (Cappellari et al. 2011a, hereinafter Paper I). In this paper, we wish to establish a census of the stellar angular momentum of ETGs in their central regions via λ_R and examine how we can relate such a measurement to their formation processes. We will show that a kinematic classification based on λ_R is a more natural and physically motivated way of classifying galaxies. More importantly, we find that galaxies classified as FRs, based on a refined criterion for λ_R , represent 86 per cent of this magnitude-limited sample of ETGs, spread over a large range of flattening, the higher end being within the range covered by spirals. SRs comprise 14 per cent of the ATLAS^{3D} sample, with about 12 per cent of massive ETGs with very low rotation and often with kinematically decoupled components, plus about 2 per cent of lower mass flattened systems which represent the special case of counter-rotating disc-like components.

In Section 2, we briefly describe the observations we are using for this study. Section 3 is dedicated to the first presentation of the measurements, mainly λ_R and its relation to other basic properties such as the ellipticity and dynamical mass. In Section 4, we use these measurements to update our view on FRs and SRs and propose a new criterion based on simple dynamical arguments. We discuss the corresponding results in Section 5 and conclude in Section 6.

2 OBSERVATIONAL MATERIAL AND ANALYSIS

The ATLAS^{3D} project is based on a volume-limited sample of 260 targets extracted from a complete sample of ETGs. A detailed description of the selection process and properties for the sample are

given in Paper I, so we only provide a summary here. The parent sample is comprised of all galaxies within a volume of 42 Mpc, brighter than $M_{K_s} = -21.5$ mag (2MASS, see Jarrett et al. 2000) and constrained by the observability ($|\delta - 29^\circ| < 35^\circ$ and away from the Galactic equatorial plane). All 871 galaxies were examined via DSS and SDSS colour images to classify them as ETGs (e.g. absence of clear spiral arms; see Paper I).

This study mostly relies on integral-field spectroscopic data from the SAURON instrument (Bacon et al. 2001) mounted on the William Herschel Telescope (La Palma, Canary Islands). We have also made use of imaging data obtained from several facilities, including the SDSS DR7 (Abazajian et al. 2009), INT and MDM (see Paper I for details). In the next section, we briefly describe the corresponding imaging and SAURON data sets and its analysis.

2.1 Photometric parameters

Various parameters were **extracted** from the imaging data at our disposal. We first derived radial profiles for all standard variables, such as the ellipticity ϵ , position angle PA_{phot} , **semimajor axis** a and disciness/boxiness as given by a_4 , from a best-fitting ellipse routine, making use of the adapted functionality in the KINEMETRY routines of Krajnović et al. (2006). The moment ellipticity ϵ profiles were computed within radially growing isophotes **via the diagonalization of the inertia tensor** as in, for example, C+07. This departs from a simple luminosity-weighted average of the ellipticity profile, which is more strongly biased towards the central values. For these profiles, we associate the ‘aperture’ radii R : **for a given elliptical aperture or isophote with an area \mathcal{A}** , R is defined as the radius of the circle having the same area $\mathcal{A} = \pi R^2$. These profiles (curves of growth) are then **interpolated** to obtain parameter values at, for example, one (or half) effective radius R_e (provided in table 5 of Paper I). To build diagrams together with quantities derived through the SAURON integral-field data (see the next section), we use ellipse and position angle profiles provided by the photometry and limit the aperture radius R to a maximum value R_S : it is the minimum between the considered radius (e.g. $1R_e$) and the radius R_{max} for which the corresponding ellipse differs in area not more than 15 per cent from the actual field coverage provided by our spectrographic data, with the ellipse itself lying at least 75 per cent within that field of view. This guarantees that we have both a good coverage in area (85 per cent) and that the SAURON spaxels reach sufficiently far out with respect to the borders of the considered aperture. Changing these criteria only affects the measured aperture values for a few systems and does not modify the global results presented here. These radial profiles were extracted from the available ground-based data. For most of the galaxies, we relied on the green g band, close to the wavelength range covered with the SAURON data cubes. For only a few galaxies, when the g -band data were not available or of poor quality, we instead relied on the red r band or even on the SAURON images reconstructed directly from the data cubes: the data used for each individual galaxy are indicated in Table B1.

A number of galaxies in our sample exhibit strong bars (e.g. NGC 936 and 6548, see Krajnović et al. 2011, hereinafter Paper II). When the galaxy is viewed at rather low inclination (close to face-on), the bar strongly influences the measured position angle (as well as the ellipticity), implying a strong misalignment between the photometric and kinematic major-axes. The (stellar) kinematic major-axis is an excellent indicator of the line of nodes of a disc galaxy, even when the galaxy hosts a relatively strong bar, and this kinematic axis generally coincides with the outer photometric major-axis outside the bar, where the light distribution is dominated by a disc. The

measured flattening does, however, not properly reflect the intrinsic flattening of the galaxy when measured in the region of the bar. In galaxies with obvious bars, such as NGC 936, 3400, 3412, 3599, 3757, 3941, 4262, 4267, 4477, 4608, 4624, 4733, 4754, 5473, 5770 and 6548, and UGC 6062, we therefore use the global kinematic position angle as derived from the two-dimensional SAURON stellar kinematics, with the moment ellipticity value from the outer parts of the galaxy (outside the region influenced by the bar; values provided in Paper II), both for the derivation of, for example, λ_R , and for all plots of this paper.

2.2 The SAURON data

The SAURON integral-field spectrograph (Integral Field Unit) has been extensively used at the Cassegrain focus of the William Herschel Telescope since 1999 (Bacon et al. 2001). All observations were conducted using the low spatial resolution mode which provides a field of view of about $33 \times 41 \text{ arcsec}^2$ and a spatial sampling of $0.94 \times 0.94 \text{ arcsec}^2$. The narrow spectral range allows the user to probe a few stellar absorption and ionized gas emission lines with a spectral resolution of about 4 \AA [full width at half-maximum (FWHM)].

All data reduction was performed using the dedicated XSAURON software wrapped in a scripted pipeline. A set of 64 galaxies included in the ATLAS^{3D} sample were observed prior to the mounting of the volume phase holographic (VPH) grating (mostly from the original SAURON survey, see de Zeeuw et al. 2002, for details). For these galaxies, we obtained an average of 2 h on source sometimes following a mosaicking strategy to cover the targets with the largest effective radii. The spectral resolution attained for these galaxies is about 4.2 \AA FWHM. For most of the 196 remaining targets, we integrated 1 h on source centred on the object, including two (slightly dithered) 30-min exposures: only when the source was extended did we allow for a mosaic of two fields to attempt to fully cover the region within $1R_e$, with two 30-min exposures for each field. The orientation of the SAURON field was adapted to each target to optimize the coverage of the galaxy, taking into account its apparent photometric flattening. The spectral resolution attained for these 196 galaxies is about 10 per cent better (due to the use of the VPH grating) and reaches 3.9 \AA FWHM.

The 260 final merged data cubes (with $0.8 \times 0.8 \text{ arcsec}^2$ rebinned spaxels) were then analysed using a common analysis pipeline and using a minimum signal-to-noise ratio threshold of 40 for the adaptive binning (Cappellari & Copin 2003). Gas and stellar kinematics were extracted via a pPXF algorithm (Cappellari & Emsellem 2004) with a library of stellar templates as in Emsellem et al. (2004), but adopting here the MILES library (Sánchez-Blázquez et al. 2006) and an optimized template per galaxy (see Paper I for details).

We derived λ_R and V/σ from growing effective apertures, as in E+07, following the ellipticity and position angle profiles obtained from the photometry or from the constant values (kinematic axes and moment ellipticity from the outer part) for galaxies with obvious bars (see Section 2.1). Using the two-dimensional spectroscopy, the expression for λ_R as given by

$$\lambda_R \equiv \frac{\langle R | V | \rangle}{\langle R \sqrt{V^2 + \sigma^2} \rangle}, \quad (1)$$

which transforms into

$$\lambda_R = \frac{\sum_{i=1}^{N_p} F_i R_i |V_i|}{\sum_{i=1}^{N_p} F_i R_i \sqrt{V_i^2 + \sigma_i^2}}, \quad (2)$$

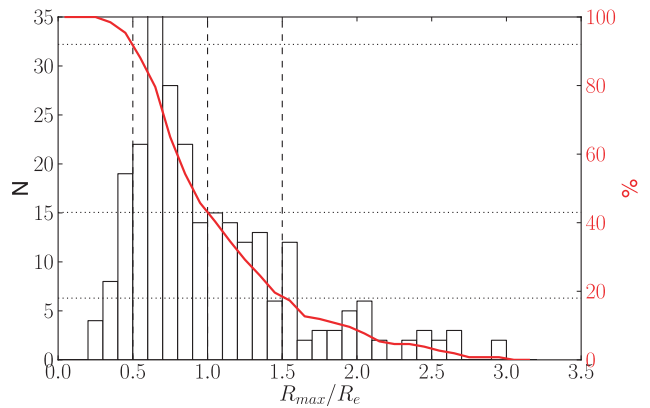


Figure 1. Histogram of the maximum aperture radius R_{\max} covered by the SAURON observations of all 260 ATLAS^{3D} galaxies (normalized by R_e). The red line shows the corresponding cumulative function (right-hand vertical scale) for galaxies with $R > R_{\max}$: we cover about 92, 43 and 18 per cent at $R_e/2$, R_e and $1.5R_e$, respectively, as indicated by the vertical/horizontal (dashed/dotted) lines.

where F_i , R_i , V_i and σ_i are the flux, circular radius, velocity and velocity dispersion of the i th spatial bin, the sum running on the N_p bins. Considering the signal-to-noise ratio threshold used here, we expect a typical positive bias for values of λ_R near zero (see appendix A of E+07) in the range $[0.025-0.05]$.

In the following, we will use λ_{R_e} and $(V/\sigma)_e$ to denote values measured at $1R_e$, and $\lambda_{R_e/2}$ and $(V/\sigma)_{e/2}$ for values at $R_e/2$. In Fig. 1, we provide an histogram of the maximum available effective aperture sizes from our SAURON data set for the ATLAS^{3D} sample: we cover an aperture of $1R_e$ or larger for 43 per cent of our sample and $R_e/2$ for 92 per cent of all ATLAS^{3D} galaxies. Note that 18 per cent are covered up to at least $1.5R_e$.

Finally, accurate dynamical masses, M_{dyn} , were derived via Multi-Gaussian Expansion (Emsellem, Monnet & Bacon 1994) of the galaxies' photometry followed by detailed Jeans anisotropic dynamical models (Cappellari 2008; Scott et al. 2009) of the ATLAS^{3D} SAURON stellar kinematics (Cappellari et al. 2010). This mass represents $M_{\text{dyn}} \approx 2 \times M_{1/2}$, where $M_{1/2}$ is the total dynamical mass within a sphere containing half of the galaxy light.

3 A FIRST LOOK AT THE APPARENT ANGULAR MOMENTUM OF ATLAS^{3D} GALAXIES

3.1 Velocity structures and λ_R

With the 260 stellar velocity maps from the ATLAS^{3D} sample, we probe the whole range of velocity structures already uncovered by E+07: regular disc-like velocity fields (e.g. NGC 4452 and 3530), kinematically distinct cores (KDCs) (e.g. NGC 5481 and 5631) or counter-rotating systems (NGC 661 and 3796), twisted velocity contours (e.g. NGC 3457 and 4552), sometimes due to the presence of a bar (e.g. IC 676, NGC 936). We also observe a few more galaxies with two large-scale counter-rotating disc-like components, as in NGC 4550 (Rubin, Graham & Kenney 1992), for example, IC 0719 or NGC 448. IC 719 exhibits in fact two velocity sign changes along its major-axis and NGC 4528 exhibits three sign changes. Only a few galaxies have noisy maps or suffer from systematics, for example, NGC 1222, UGC 3960 or PGC 170172, due to the low signal-to-noise ratio of the associated data cubes or from intervening structures (e.g. stars). The reader is referred to

Paper II for further details on the kinematic structures present in galaxies of the ATLAS^{3D} sample.

The ATLAS^{3D} sample of ETGs covers λ_{Re} values from 0.021 for M87 (NGC 4486), therefore consistent with the zero apparent angular momentum within the SAURON field of view, and 0.76 for NGC 5475, a flattened disc-like galaxy. Other galaxies with low λ_{Re} values and stellar velocity fields with the nearly zero-velocity amplitude (within the noise level) are NGC 3073, 4374, 4636, 4733, 5846 and 6703. Of these six, NGC 4374, 4636 and 5846 are nearly round, massive galaxies with a mass well above $10^{11} M_{\odot}$ and strong X-ray emitters. NGC 4636 shows a very low amplitude velocity field and a barely detectable kinematically distinct component. There are two more galaxies with significantly non-zero values of λ_{Re} (~ 0.1), but no detectable rotation, the relatively high λ_{Re} values being due to larger uncertainties in the kinematics: NGC 3073 and 4733. Along with NGC 6703, these galaxies stand out as galaxies with no apparent rotation, a mass below $10^{11} M_{\odot}$ and an effective radius smaller than 3 kpc: these are very probably nearly face-on disc galaxies (NGC 4733 being a face-on barred galaxy).

If we use the previously defined threshold separating SRs and FRs, namely $\lambda_{Re} = 0.1$, we count a total of 23 galaxies below that limit in our sample, a mere 9 per cent of the full ATLAS^{3D} sample. This is to be compared with one-fourth (25 per cent) of galaxies below that threshold found in E+07 within the representative SAURON sample of 48 ETGs (de Zeeuw et al. 2002). With the ATLAS^{3D} project, we are covering a complete volume-limited sample, more than five times larger than the original SAURON sample, but we less than double the number of such slowly rotating objects. This is expected considering that such galaxies tend to be on the high-luminosity end (E+07; C+07). A volume-limited sample includes far more galaxies in the low-luminosity range than the SAURON representative sample which had a flat luminosity distribution. Our ATLAS^{3D} observations confirm the fact that SRs and FRs are not distributed **evenly** in the absolute magnitude: fast-rotating systems brighter than $M_{K_s} = -24$ are rare, while a third of all galaxies having $\lambda_{Re} \leq 0.1$ are in this range. This is **emphasized** in Fig. 2 where the *K*-band luminosity histograms for galaxies in bins of λ_{Re} are presented. **This trend could be due to an incomplete field coverage of the brighter galaxies with large R_e when λ_R increases outwards** (we reach $1R_e$ for only about 42 per cent, see Fig. 1, and this is obviously biased towards the fainter end of galaxies). However, this trend is still present when using λ_R at $R_e/2$ (bottom panel of Fig. 2) for which we have about 92 per cent of all galaxies properly covered.

Among the 23 galaxies with $\lambda_{Re} \leq 0.1$ in the ATLAS^{3D} sample, six have no detected rotation (three of them being very probably face-on disc-like systems, see above), two have twisted or prolate-like isovelocity contours (NGC 4552 and 4261) and out of the remaining 15 others, 14 have KDCs (see Paper II), confirming the claim made in E+07 that most ETGs with low λ_R values have KDCs.

3.2 ATLAS^{3D} galaxies in a λ_R - ϵ diagram

The combination of the measured λ_{Re} values with the apparent flattening ϵ_e holds important clues **pertaining** to the intrinsic morphology and dynamics of ETGs, as shown in E+07. In Fig. 3, we provide the first **glimpse** at the distribution of galaxies in such a λ_R - ϵ diagram for an aperture radius of $1R_e$.

A more standard approach includes the use of (V/σ) as a probe for the stellar kinematics of galaxies. In C+07, it has been shown that there seems to be a broad trend between the anisotropy of

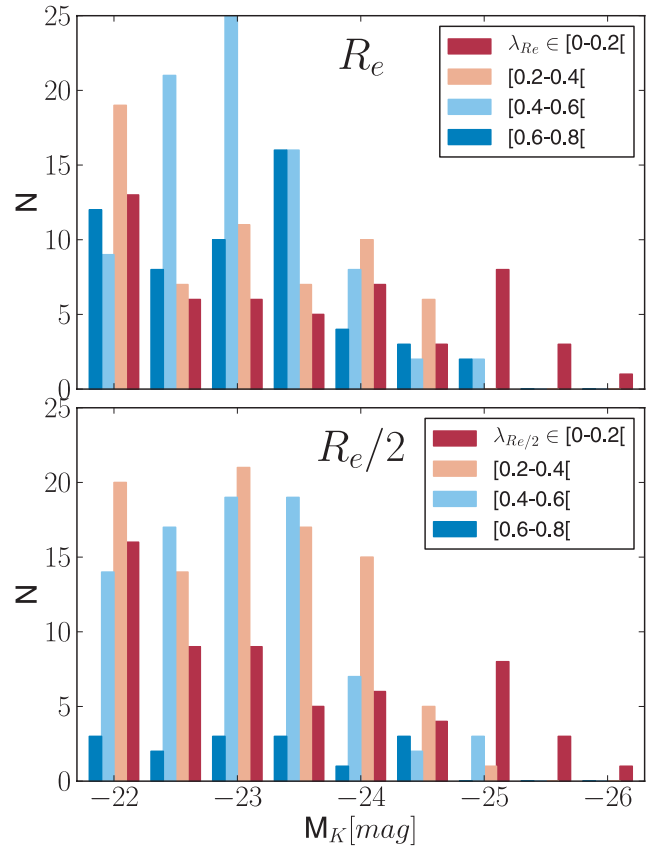


Figure 2. Histograms of *K*-band luminosities for all 260 ATLAS^{3D} galaxies, in bins of λ_{Re} (red: [0–0.2]; light red: [0.2–0.4]; light blue: [0.4–0.6]; blue: [0.6–0.8]). The top panel uses λ_R values derived for an aperture radius of $1R_e$ and the bottom panel uses λ_R values derived for an aperture radius of $R_e/2$.

ETGs, parametrized¹ with β , and their intrinsic (**edge-on**) ellipticity ϵ_{intr} . FRs were found to be generally distributed on the (V/σ) - ϵ diagram within the **envelope** traced by the edge-on relation $\beta = 0.7 \times \epsilon_{intr}$ (from the analytic formula of Binney 2005) and by its variation with the **inclination** (fig. 11 of C+07). This analytic relation is nearly identical to $\beta = 0.65\epsilon$, which includes the aperture integration within $1R_e$ (Appendix B). Since V/σ and λ_R of simple ellipsoidal systems (with constant anisotropy) can be linked via a relatively simple formula (see Appendix B), we can translate these β - ϵ_{intr} relations for λ_R and provide the corresponding curves in a λ_R - ϵ diagram. These relations are shown in Fig. 3 for edge-on galaxies (dashed and solid magenta lines) as well as the effect of inclination (dashed black lines, only for the relation integrated within $1R_e$).

We first confirm that most of the galaxies with λ_{Re} values significantly above 0.1 are located above (or at the left-hand side of) the magenta line in Fig. 3. The dashed line at $\epsilon_{intr} = 0.85$ also provides a convenient upper envelope of the galaxies in our sample. This beautifully confirms the predictions made in C+07, using only a small set of targets, and reveals important characteristics of the internal state of ETGs, which will be further discussed in Section 5.1.

¹ β is the anisotropy parameter simply defined as $1 - \sigma_z^2/\sigma_R^2$ for a steady-state system where σ_R and σ_z are the cylindrical components of the stellar velocity dispersion.

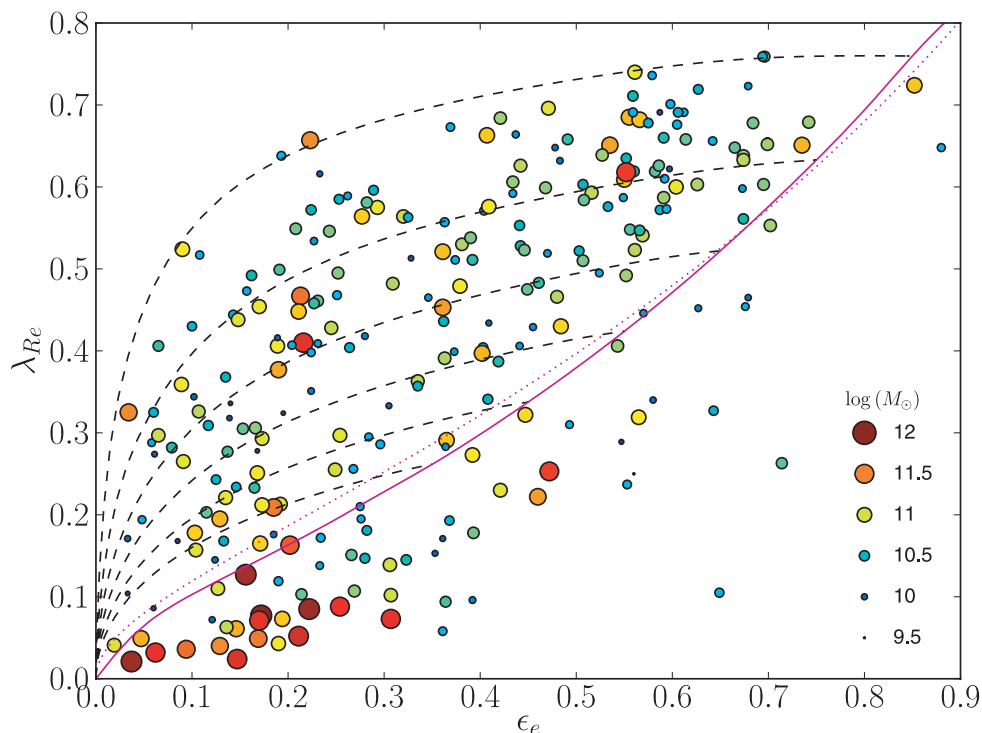


Figure 3. $\lambda_{R\epsilon}$ versus the ellipticity ϵ_e for all 260 ATLAS^{3D} galaxies. The colour and size of the symbols are associated with the mass of each galaxy, as indicated at the bottom right-hand corner of the panel. The dotted magenta line shows the edge-on view for ellipsoidal galaxies integrated up to infinity with $\beta = 0.70 \times \epsilon$, as in C+07. The solid magenta line is the corresponding curve restricted to an aperture at $1R_e$ and for $\beta = 0.65 \times \epsilon$ (see text for details). The black dashed lines correspond to the location of galaxies with intrinsic ellipticities $\epsilon_{\text{intr}} = 0.85, 0.75, 0.65, 0.55, 0.45$ and 0.35 along the relation given for an aperture of $1R_e$ with the viewing angle going from edge-on (on the relation) to face-on (towards the origin).

The majority of galaxies above the magenta line are consistent with intrinsic ellipticities between 0.55 and 0.85, with only very few galaxies below $\epsilon_{\text{intr}} = 0.35$. The stellar velocity maps of these fast-rotating objects, illustrated in Fig. 4 with six examples of galaxies from low (~ 0.35 , bottom) to high (~ 0.85 , top) ellipticities along the magenta line, are regular and show disc-like signatures (e.g. pinched isovelocity contours), strongly in contrast to the complex kinematic features observed for galaxies with low $\lambda_{R\epsilon}$ values, as discussed in Section 3.1: this is objectively quantified in Paper II. We here probe from very flattened edge-on cases dominated by a thin disc component at the top to relatively fatter objects like NGC 4621 at the bottom. All six galaxies exhibit a clear sign of a disc-like component from flattened isophotes and/or pinched isovelocities, confirming the fact that they cannot be viewed far from edge-on.

The distribution of galaxies in the ATLAS^{3D} sample in the λ_R - ϵ plane also reveals a rather well-defined upper envelope: as the ellipticity decreases, the maximum apparent angular momentum decreases accordingly. It can be understood by looking at Fig. 3 again where the upper black dashed line corresponds to an extremely flattened spheroid with $\epsilon_{\text{intr}} = 0.85$ (a disc) and an anisotropy parameter of $\beta = 0.55$ (following the β - ϵ_{intr} relation mentioned above): most galaxies in the ATLAS^{3D} sample have lower λ_R .

This first view at the distribution of the ATLAS^{3D} galaxies in a λ_R - ϵ diagram provides a very significant upgrade on already published samples. We can therefore now proceed by combining the detailed study of the kinematic structures observed in these galaxies conducted in Paper II with such information to deliver a refined criterion for disentangling FRs and SRs.

4 GALAXY CLASSIFICATION VIA STELLAR KINEMATICS

4.1 The importance of shapes

We have seen in the previous section that galaxies with the lowest λ_R values tend to be more luminous or massive (see Figs 2 and 3) and exhibit complex kinematic structures, as opposed to fast-rotating galaxies with regular velocity fields and disc-like signatures (when viewed near edge-on). This confirms the view delineated in E+07 and C+07, where early-type systems were separated into two families, the so-called FRs and SRs. However, it is not clear whether a constant value of λ_R (e.g. $\lambda_R = 0.1$ as defined in E+07 from a representative sample of 48 galaxies) corresponds to the best proxy for distinguishing between SRs and FRs.

Using the complete ATLAS^{3D} sample of 260 galaxies, we can in fact proceed with an improved criterion, taking into account the fact that two galaxies with the same apparent angular momentum but very different (intrinsic) flattening must have, by definition, a different orbital structure. A galaxy with a relatively low value of λ_R , for example, 0.2, may be consistent with a simple spheroidal axisymmetric system viewed at a high inclination (near face-on), but this is true only if its ellipticity is correspondingly low: a large ellipticity, for example, $\epsilon = 0.4$, would imply a more extreme object (in terms of the orbital structure or anisotropy), as shown with the spheroidal models provided in Appendix B.

This can be further illustrated by looking at Fig. 5 where the radial λ_R profiles are shown for all galaxies of the sample in bins of ellipticities. For low ellipticities, $0 < \epsilon < 0.2$, there is a rather

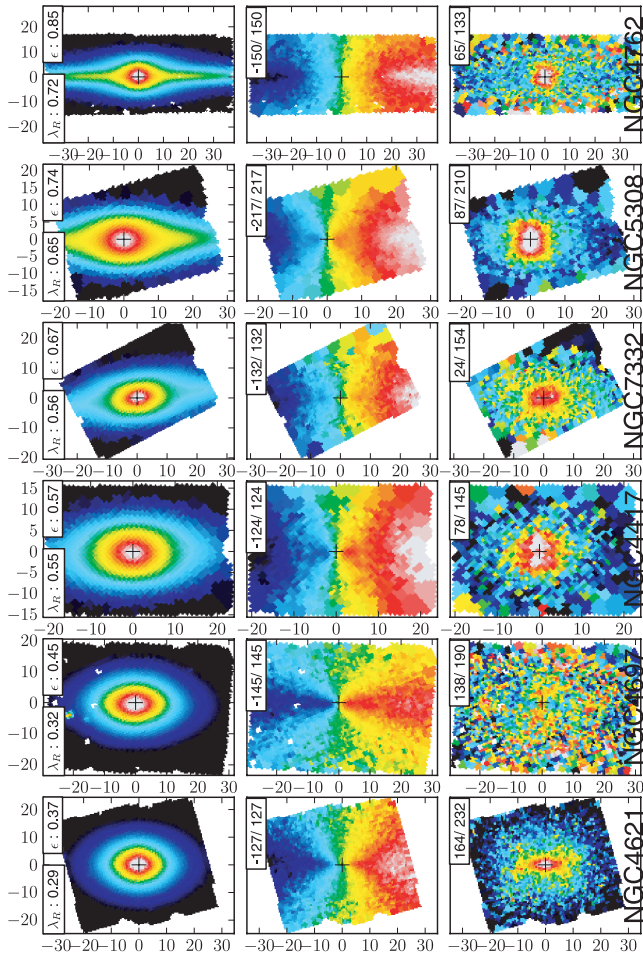


Figure 4. Reconstructed images and first two stellar velocity moment maps (velocity and velocity dispersion) for six galaxies selected near the ellipticity–anisotropy relation (magenta line, see text). The apparent ellipticity is decreasing from the top to bottom.

continuous sequence of profiles with various λ_R amplitudes from 0.1 to 0.5 at $1R_e$: a rather face-on flattened system would have a profile similar to an inclined mildly-triaxial galaxy. In the next bin of ellipticities, $0.2 < \epsilon < 0.4$, we start discerning two main groups of galaxies: the ones with rapidly increasing λ_R profiles, most of these galaxies showing regular and symmetric velocity fields (as in Fig. 4), and those which have flatter (or even decreasing) profiles up to $\sim R_e/2$ and then start increasing outwards, again often exhibiting complex velocity maps and distinct central stellar velocity structures. There are in addition a few galaxies with λ_R profiles going up to ~ 0.3 and *decreasing* between $R_e/2$ and R_e . As we reach the last ellipticity bin (with the highest values), most galaxies have strongly rising λ_R profiles reaching typical values of $\lambda_R \sim 0.5$ at $R_e/2$. The three galaxies which have λ_{Re} below 0.4 are IC 719, NGC 448 and the famous NGC 4550, all being extreme examples of disc galaxies with two counter-rotating systems.

A refined scheme to separate slow- and fast-rotating galaxies should therefore take into account the associated apparent ellipticity: we should expect a higher value of the specific stellar angular momentum for galaxies which are more flattened or closer to edge-on if these are all intrinsically FRs. Very flattened galaxies with λ_{Re} as low as 0.2 or 0.3 must already have a rather extreme orbital distribution (or strong anisotropy, see Appendix B). In the next section, we use the completeness of our sample of ETGs to revisit the

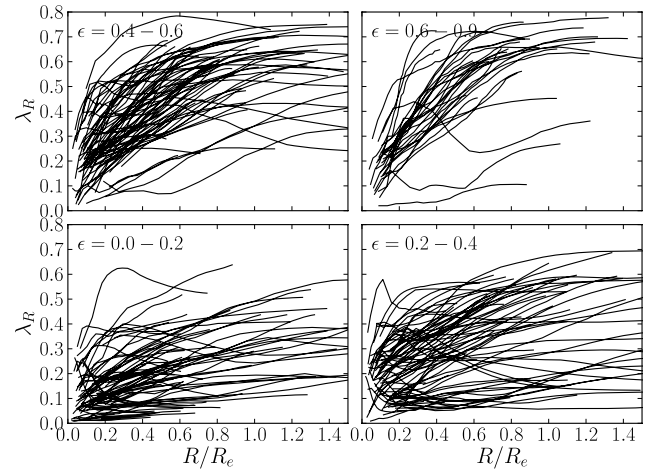


Figure 5. λ_R profiles for the complete ATLAS^{3D} sample of early-type galaxies, in four bins of ellipticities ϵ_e (as indicated in each panel), as a function of the aperture radius (relative to the effective radius R_e).

question of how to distinguish members of the two main families of ETGs, namely SRs and FRs.

4.2 Kinematic structures and the link with λ_R

The classification of ETGs into SRs and FRs was motivated by the (qualitative) realization that galaxies within the SAURON sample of 48 ETGs (de Zeeuw et al. 2002) exhibit either the regular stellar rotation, showing up as classical ‘spider diagrams’, with no significant misalignment between the kinematic and photometric axes (excluding the few systems consistent with having no apparent rotation at all), or complex/irregular stellar velocity maps with twists and strong misalignment with respect to the photometry (Emsellem et al. 2004; Krajnović et al. 2008). Using λ_R as a proxy to disentangle the two families of objects, it was confirmed that these two families had distinct structural and dynamical properties (E+07; C+07).

We can now review these results in the context of our complete ATLAS^{3D} sample: this requires an objective assessment of the observed kinematic structures. **The regularity or richness of a velocity map can be defined and more importantly quantified using KINEMETRY** (Krajnović et al. 2006). Such an evaluation has thus been conducted in Paper II systematically for all 260 ATLAS^{3D} galaxies. The (normalized) amplitude of the fifth harmonic kinematic term k_5 (k_5/k_1) can, for example, be used to find out whether or not a velocity field has isovelocity contours consistent (in azimuth) with the cosine law expected from pure disc rotation. **The fact that the velocity map of a galaxy follows the cosine law does not directly imply that it is a pure-disc system, only that its line-of-sight velocity field looks similar to one of a two-dimensional disc.** Using a threshold of 4 per cent for k_5/k_1 , galaxies with or without regular velocity patterns have been labelled in Paper II as regular and non-regular rotators, respectively, and provided a detailed and quantified account of observed velocity structures. Galaxies such as NGC 3379 or 524 exhibit low-amplitude rotation but are consistent with being regular rotators, while galaxies like NGC 4406 or 4552 are clearly non-regular rotators (see figs B1, B5 and B6 of Paper II) even though these are rather round in projection.

All 260 galaxies of the ATLAS^{3D} sample are shown with symbols for regular and non-regular rotators in Fig. 6: we plot both measured V/σ_e and λ_{Re} as functions of ϵ_e . The expected locations for systems

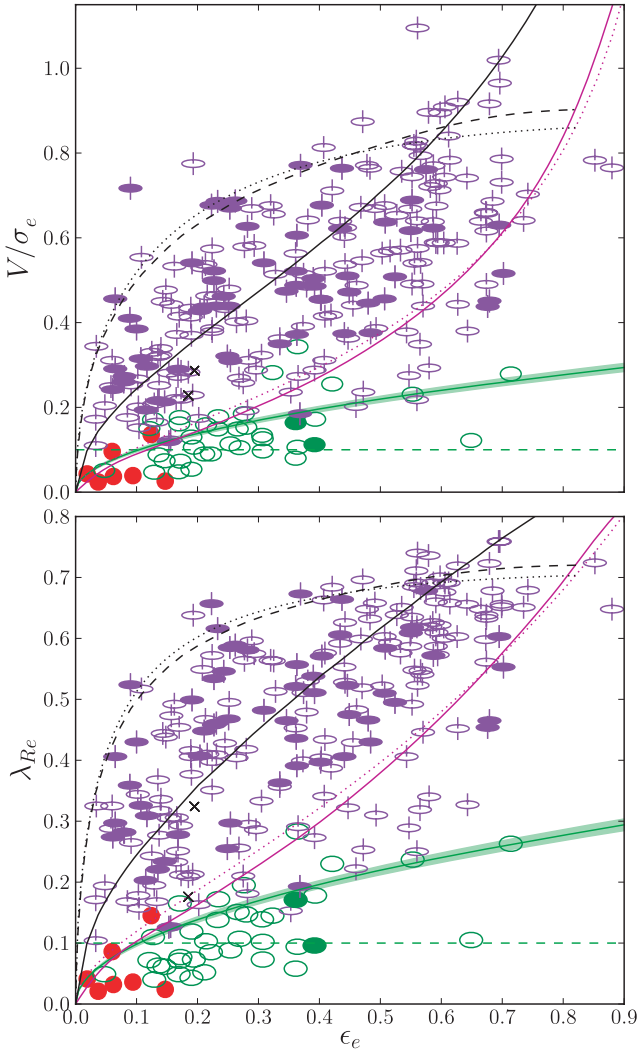


Figure 6. Measured V/σ_e (top panel) and λ_{Re} (bottom panel) values versus the ellipticity ϵ_e within an aperture of $1R_e$. The magenta lines are as in Fig. 3 and the black dotted and dashed lines represent the location of galaxies with an intrinsic ellipticity $\epsilon = 0.82$ when going from an edge-on to a face-on view. The solid black line corresponds to isotropic oblate systems viewed edge-on. The solid green line is $0.31 \times \sqrt{\epsilon}$. The red circles are galaxies with no apparent rotation, and the green ellipses and purple symbols are for non-regular rotators and regular rotators, respectively. The filled symbols correspond to galaxies with bars. Regular and non-regular rotators are better separated using λ_R than V/σ .

with $\beta = 0.7 \times \epsilon$, where β is the anisotropy parameter, are presented as the dotted lines, the magenta line representing edge-on systems and the dashed black line showing the effect of the inclination for an intrinsic (edge-on) ellipticity of 0.82. These curves are calculated following the formalism in Binney (2005) and the specific values are identical to the ones defined in C+07. We also provide similar relations for $\beta = 0.65 \times \epsilon$ as in Fig. 3, but this time taking into account the effect of a limited aperture ($1R_e$).

We observe in Fig. 6 that regular rotators tend to have V/σ or λ_R values above the magenta line. This clearly confirms the trend emphasized in C+07 already obtained with a significantly smaller sample. The ATLAS^{3D} sample clearly extends this result to galaxies at higher ellipticities and V/σ or λ_R values. The second obvious and complementary fact is that non-regular rotators cluster in the lower part of the diagrams and below the magenta line. Overall,

this shows that objects with or without specific kinematic features in their velocity or dispersion maps tend to be distributed on either side of the relation illustrated by the magenta line.

This strongly suggests that the regularity of the stellar velocity pattern is closely related to the SRs and FR classes, as defined in E+07, and that the ATLAS^{3D} sample of 260 galaxies provides the first view of a complete sample of ETGs, expanding on the perspective derived from the original SAURON sample of 48 galaxies. We do not expect a one-to-one relation between non-regular rotators and SRs, on the one hand, and regular rotators and FRs, on the other hand, because any departure from a regular disc-like rotation automatically qualifies a galaxy as a non-regular rotation pattern. However, apart from atypical cases, such as unrelaxed merger remnants or galaxies with strong dust features, we may expect that such a link holds. We now examine how to best separate these two families of ETGs.

4.3 Slow and fast rotators

The V/σ diagram (Fig. 6) shows, independently of any refined criterion to disentangle regular and non-regular rotators, significantly higher overlap between the two populations both at low and high ellipticities. The difference between V/σ and λ_R may not, however, be that obvious by just looking at Fig. 6. For simple oblate models, as illustrated in Appendix B, there is a tight correlation between these two quantities (see Fig. B1). This is not the case anymore when the galaxy exhibits more complex kinematics with, for example, a rapidly rotating inner part and a slowly rotating outer part. Two galaxies with apparent dynamics as different as between NGC 5813 and 3379 have similar V/σ values, although the latter is a regular rotator, while the former is a non-regular rotator with a clear stellar KDC (see E+07). In this context, λ_R is a better discriminant and this occurs because the weighting of the stellar rotation depends both on the observed flux and on the size (radius) of the structure. While the difference may not be dramatic and would not impact the majority of ETGs (since most have regular stellar velocity fields), it becomes relevant when considering classes of galaxies for which we observe differences in the observed kinematic features. This has motivated the use of λ_R which also directly relates to the apparent angular momentum of the stars (E+07).

Before we refine the above-mentioned criterion, we need to emphasize again the clear trend observed in the λ_R – ϵ diagram (bottom panel of Fig. 6): galaxies have on average increasing values of λ_R as the ellipticity increases and this is valid also for non-regular rotators alone. As mentioned in Section 4.1, at a constant λ_R value, the anisotropy increases with higher ellipticities, and we therefore need to define a threshold for slow/FRs which depends on and increases with the ellipticity.

We considered several possibilities, including scaled-down versions of the predicted λ_R – ϵ relation for isotropic axisymmetric systems or of the magenta lines. The first one (isotropy being used as a reference) does a reasonable job at separating regular and non-regular rotators, with a scaling factor of ~ 0.4 and would naturally connect our study with already published work. The fact that galaxies with low V/σ or λ_R exhibit different observed properties is certainly not a new result and was illustrated and emphasized in a number of key studies (e.g. Bender 1988; Kormendy & Bender 1996) using the ratio V/σ_* between the measured V/σ and the predicted value from an oblate isotropic rotator V/σ_{iso} (see e.g. Davies et al. 1983). V/σ_* has thus sometimes been used as an indication of an anisotropic dispersion tensor: this view is in fact misleading as a constant value for V/σ_* does imply an increasing anisotropy with

increasing flattening (C+07). This statement is also valid for $\lambda_{R_*} = \lambda_R/\lambda_{\text{Riso}}$ obviously for the same reason.

More importantly, C+07 have shown that **galaxies can generally not be considered as isotropic** (see Fig. 6). **Global anisotropy increases with the intrinsic flattening**, therefore using isotropic rotators as a reference for flattened galaxies would not be appropriate. Galaxies in the ATLAS^{3D} sample appear to be distributed around the isotropy line in Fig. 6, but this relation is derived for *edge-on* systems, and galaxies should span the full range of inclinations with roughly as many galaxies above and below an inclination of 60°. Scaling of the magenta line would in this context be more appropriate, although it clearly has a similar drawback: it is defined for intrinsically edge-on systems, does not follow the variation of λ_R and ϵ due to inclination effects and therefore does not perform well in disentangling regular rotators from non-regular ones.

After considering various possibilities, we finally converged on what we believe is the simplest proxy which can properly account for the two observed families, minimizing the contamination on both sides. We therefore fixed the threshold for λ_R to be proportional to $\sqrt{\epsilon}$ with a scaling parameter k_{FS} which depends on the considered apertures, namely

$$\lambda_{R_e} = (0.31 \pm 0.01) \times \sqrt{\epsilon_e}, \quad (3)$$

$$\lambda_{R_e/2} = (0.265 \pm 0.01) \times \sqrt{\epsilon_{e/2}}. \quad (4)$$

The different values of k_{FS} for these two apertures obviously follow the observed mean ratio between λ_{R_e} and $\lambda_{R_e/2}$ (see Appendix B). Here, λ_R and ϵ are *measured* values: formal errors for these are very small (because these parameters are computed using many independent spaxels). Uncertainties in the measurements of λ_R are thus mostly affected by systematic errors in the stellar kinematic values and are difficult to assess. The quoted ranges in equations (3) and (4) [0.30–0.32] and [0.255–0.275] for R_e and $R_e/2$, respectively) are therefore only indicative of the difficulty in defining such empirical thresholds. The relation for a $1R_e$ aperture is shown as a solid green line (the filled area showing the quoted ranges) in Fig. 6: **it performs well in its role to separate galaxies with regular and non-regular velocity patterns**, and does slightly better with λ_R than with V/σ which shows a 50 per cent increase in misclassified objects (and a larger number of non-regular rotators above the magenta line). The two non-rotators which are above the green line (NGC 3073 and 4733; red circles) are in fact very probably face-on fast-rotating galaxies.

Equations (3) and (4) can therefore be used to define FRs and SRs, but as for any classification scheme, we need to define a scale at which to apply the criteria: this is further examined in the next Section.

4.4 The importance of a scale

Large-scale structures ($\sim 2R_e$ and beyond) are certainly important to understand the formation and assembly history of galaxies, and reveal, for example, signatures such as faint tidal structures or streams. However, we are interested here in probing the central regions of ETGs, at the depth of their potential wells where metals are expected to have accumulated or been produced, and where stellar structures should have had time to dynamically relax: using apertures of one effective radius follows these guidelines and, moreover, covers about 50 per cent of the stellar mass.

The stellar angular momentum is generally observed to increase at large radii (E+07), even for SRs, and this is also valid for most

ATLAS^{3D} galaxies (Fig. 5). The majority of fast-rotating galaxies reach close to their maximum λ_R values between $R_e/2$ and R_e : beyond that radius, the profiles often smoothly bend and reach a plateau. Many galaxies with low central apparent angular momentum also show λ_{R_e} increasing values outside $R_e/2$. It is also true that most kinematically distinct components observed in our ATLAS^{3D} sample have radii smaller than $R_e/2$ and for all the detected KDCs in our sample, the maximum radius covered is at least 50 per cent larger than the radius of the KDC itself. This suggests that **both apertures of $R_e/2$ and R_e could serve as reference scales to define SRs and FRs** (hereinafter SRs and FRs, respectively). Using apertures smaller than $R_e/2$ is not advised, as this would make the measurements more dependent on instrumental characteristics and observation conditions, and would probe only the core regions. To compare how our criterion performs for $1R_e$ and $R_e/2$, we will use a more detailed description of the kinematic features present in the maps: this will help interpret the observed similarities and differences.

In Paper II, the regular/non-regular rotator types, which globally define the observed velocity structure of a galaxy (in combination with key features observed in both the velocity and velocity dispersion maps and analysed via KINEMETRY), have been used to define five kinematic groups:

- (i) *Group a*: galaxies with no apparent rotation or non-rotators (seven members);
- (ii) *Group b*: galaxies with the non-regular velocity pattern (non-regular rotators), but without any specific kinematic feature (12 members);
- (iii) *Group c*: galaxies with KDCs or counter-rotating cores (19 members);
- (iv) *Group d*: galaxies with two symmetrical off-centred stellar velocity dispersion peaks (11 members);
- (v) *Group e*: galaxies with the regular apparent rotation (regular rotators) and with or without small minor-axis kinematic twists (209 members).

Galaxies of groups a–d are mostly non-regular rotators, while most of the galaxies in group e are regular rotators. Galaxies of *group d*, also called ‘ 2σ ’ galaxies due to the appearance of their velocity dispersion maps, are interpreted as systems with two counter-rotating flattened stellar components which can have various relative luminosity contributions. This includes galaxies such as the well-known NGC 4550 (Rubin et al. 1992), which is made of two counter-rotating discs of nearly equal light (Rix et al. 1992; C+07) and for this reason ends up as a SR, or other cases like NGC 4473, which has a smaller amount of counter-rotating stars (C+07) and thus appears as a FR, or newly discovered objects like NGC 4528 (Paper II). Among our sample of 260 objects, two galaxies could not be classified due to the low signal-to-noise ratio of the extracted kinematics.

In Fig. 7, we now re-examine the λ_R values for our ATLAS^{3D} sample in light of these five *kinematic groups* for both apertures of R_e and $R_e/2$. As expected, both the ellipticity ϵ and λ_R values are smaller within $R_e/2$: λ_R is generally an increasing function of the radius and going inwards we tend to shift away from a large-scale disc structure when present (the median of our observed $\lambda_{R_e}/\lambda_{R_e/2}$ values is ~ 1.17 ; see also Appendix B). All results previously mentioned within an aperture of $1R_e$ are confirmed with a smaller one ($R_e/2$). The galaxies of *kinematic groups a, b, c* and *d* seem to nicely cluster below the green lines defined in equations (3) and (4), and the resulting separation of these targets from the *kinematic group e* (regular rotator) is marginally sharper within $R_e/2$: there are no

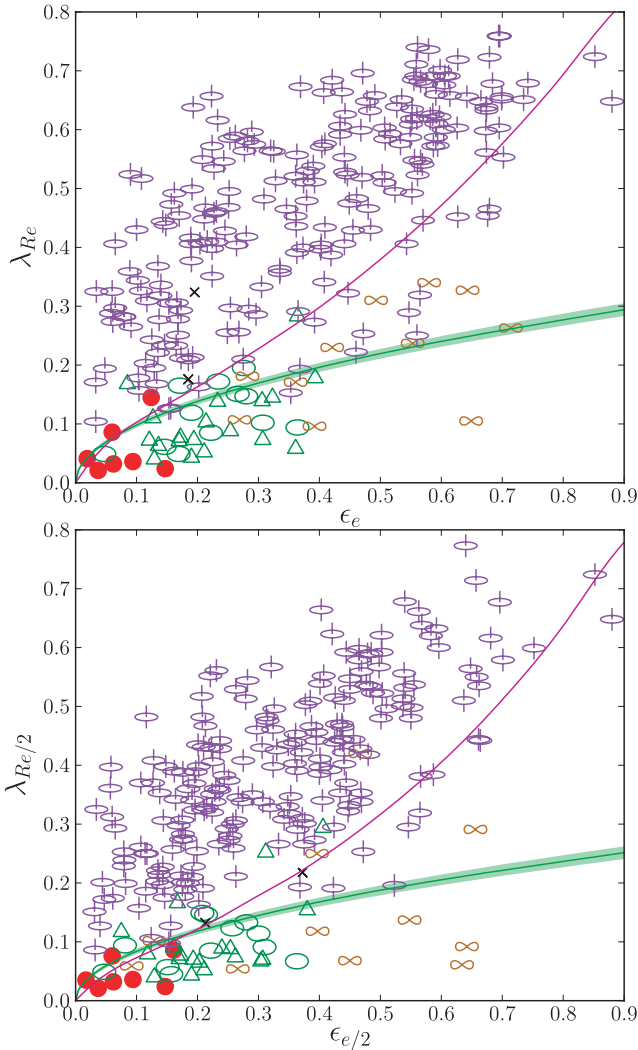


Figure 7. As in the bottom panel of Fig. 6, but here for λ_R within apertures of R_e (top panel) and $R_e/2$ (bottom) panel. The symbols correspond to different kinematic groups (see text for details): red circles are for non-rotators, green ellipses are for non-regular rotators without any specific kinematic feature, green triangles are for galaxies with KDCs, orange lemniscates are for 2σ galaxies (galaxies with two counter-rotating flattened stellar components), purple symbols are for regular rotators and black crosses are for two galaxies which could not be classified.

galaxies of *group e* below the green line and most 2σ galaxies are now below the defined threshold for SRs.

Equations (3) and (4) thus provide excellent (and simple) proxies to discriminate between galaxies of *kinematic groups a, b, c, d* and *e*, or conversely between regular and non-regular rotators, with only one object with regular disc-like stellar velocity maps below the line (NGC 4476) at $1R_e$ and none for the smaller aperture. In fact, NGC 4476 seems to be a bona fide *group d* galaxy, but with an unusually large inner counter-rotating component (Alison Crocker, private communication).

Using these criteria, there are 36 SRs out of 260 for an aperture of R_e and 37 for $R_e/2$, with 30 in common for both apertures. All targets which change the class going from $R_e/2$ to R_e are well covered with the available SAURON field of view and this is therefore not an effect of the spatial coverage. Galaxies which are FRs at $R_e/2$ and SRs at R_e are NGC 4476, 4528 and 5631, PGC 28887 and UGC 3960 and those being SRs at $R_e/2$ and FRs at R_e are IC 719,

NGC 770, 3073, 3757, 4259, 4803 and 7710. All except two of these are either near the dividing line or specific cases, such as, again, NGC 4550-like systems. The two discrepant cases, namely NGC 4476 and PGC 28887, have central decoupled kinematic components with a radial size larger than $R_e/2$. The fact that 2σ galaxies change the class and that we still have some of them above the threshold even within $R_e/2$ (NGC 448 and 4473) is expected, as the corresponding counter-rotating components span a range of the spatial extent and luminosity contribution which directly affect the λ_R measurements: 2σ galaxies which are SRs have a high enough contribution within the considered aperture to significantly influence the measured stellar angular momentum.

As mentioned, 30 out of 36 SRs at R_e are also SRs at $R_e/2$: for 22 of these, the SAURON data do not reach $1R_e$. Considering a simple extrapolation of their λ_R profiles (see also E+07), there is little chance that any of these cross the threshold between SRs and FRs at R_e . We therefore advocate the use of one effective radius R_e as the main scale to probe FRs and SRs, considering that doing so focuses the classification on a central but fixed and significant fraction (50 per cent) of its luminosity.

By defining our classification criteria to such central regions, we may be weighting more towards dissipative processes and consequently avoiding regions dominated by the dry assembly of galaxies (Khochfar & Burkert 2003) which is thought to mostly affect the outer parts (Naab et al. 2007; Hopkins et al. 2009b; Naab, Johansson & Ostriker 2009; Bois et al. 2010; Hoffman et al. 2010; Oser et al. 2010). We may also consequently miss very large KDCs (Coccato et al. 2009) or, for example, any outer signature of interaction. This should obviously be kept in mind when interpreting the results: depending on the formation and assembly history, we expect galaxies to have significantly different radial distribution of their stellar angular momentum.

The use of an aperture radius of $1R_e$ is motivated by the following facts: it has discriminating power, as shown in the previous section, and we expect differences to be apparent in simulations (see Section 5.3); such a scale is accessible to integral-field spectroscopy as well as modern numerical simulations; it is too large to significantly suffer from variations in the observational conditions (e.g. seeing); it traces a significant fraction of the stellar mass, namely about 50 per cent for systems with shallow spatial variations of their stellar populations. We note here that we obtain consistent results with a smaller aperture, $R_e/2$, besides the change in the class for a few flattened SRs from the 2σ kinematic group. We acknowledge, however, that this consistency may not hold for arbitrarily large apertures, even though the criterion itself is a function of the aperture size.

Our refined criterion is motivated to respect the relation between the dynamical structure and apparent shape, which should increase its robustness to, for example, the changing rotation at different radii. We also note that the criterion itself is empirically determined and changes depending on the scale used. One should avoid using the distribution measured at, for example, R_e , to classify galaxies based on data from grossly different spatial scales. It is also critical for any comparison of simulations with observed galaxies to measure these parameters consistently, using the same spatial extent.

4.5 Robustness of the new classification scheme

The new proxy for SRs and FRs differs from the previous constant threshold criterion in two main ways. First, at high ellipticities, it reaches higher λ_R values (~ 0.25 for $\epsilon = 0.8$). Secondly, the new relation goes to zero for very low ellipticities (apparently round

galaxies). The three non-rotators (red circles in Fig. 6) which are close to the defined relation are all very probably nearly face-on rapidly rotating galaxies which would be significantly above the line were they viewed edge-on. For a FR to be consistent with no rotation requires very low inclination and therefore extremely round isophotes (see e.g. Jesseit et al. 2009). The new relation works significantly better at disentangling such cases from the truly low-angular-momentum galaxies. This partly comes from the fact that the dependency on the ellipticity (criterion $\propto \sqrt{\epsilon}$) somewhat mimics the variation in λ_R and ϵ due to inclination effects.

The new criterion defined should minimize the contamination and misclassification, but as for any empirically designed classification, we expect some ambiguous cases or systems for which it is hard to conclude. There are, for example, two galaxies, namely NGC 5173 and 3757, which coincidentally have the same $\lambda_{Re}/2$ and $\epsilon_{e/2}$, and lie at the very limit between SRs and FRs (NGC 3757 is in fact a galaxy with a bar which perturbs the ellipticity measurement). Three non-regular rotators are significantly above the curve (to be compared with the total of 224 FRs), namely NGC 770, 5485 and 7465: NGC 770 is a galaxy with a known counter-rotating disc (Geha, Guhathakurta & van der Marel 2005), NGC 5485 is one of the rare galaxies with prolate kinematics (as NGC 4621) and NGC 7465, which is the non-regular rotator with the highest λ_{Re} value, is an interacting system forming a pair with NGC 7464 (Li & Seaquist 1994) and shows a complex stellar velocity field with a misaligned central disc-like component.

The probability of a galaxy to be misclassified as a slow (or fast) rotator is hard to assess. We can at least estimate the uncertainty on the number of SRs in our sample by using the uncertainty on the measurements themselves (λ_R and ϵ), the observed distribution of points and the intrinsic uncertainty in defining the threshold for $\lambda_R^N = \lambda_R/\sqrt{\epsilon}$. Using R_e as the reference aperture, we estimate the potential contamination of SRs by FRs by running Monte Carlo simulations on our sample (assuming Gaussian distribution for the uncertainty on ϵ and λ_R of 0.05) to be ± 6 galaxies (2σ). We obtain a relative fraction of $\sim 14 \pm 2$ per cent of SRs in the full ATLAS^{3D} sample of ETGs, which represents 4 per cent of the full parent sample of 871 galaxies (Paper I). This is much lower than the 25 per cent quoted in E+07, but as mentioned above, this is due to the flatness of the luminosity distribution of the original SAURON sample.

4.6 Slow rotators, fast rotators and Hubble types

We now examine the Hubble-type classification in light of our new scheme to separate FRs and SRs. In Fig. 8, we show the distribution of galaxies in the λ_R – ϵ diagram using the two main classes of Es ($T < -3.5$) and S0s ($T \geq -3.5$, as defined in Paturel et al. 2003).

The ATLAS^{3D} sample of 260 ETGs includes 192 S0s and 68 Es. As expected, Es in the ATLAS^{3D} sample tend on average to be more massive and rounder than S0s. We therefore naturally retrieve the trend that Es tend to populate the left-hand part of the diagram and within the SR class, there is a clear correlation between the apparent ellipticity and being classified as an E or S0, the latter being all more flattened than $\epsilon = 0.2$. Es also tend to be in the lower part of the diagram (low value of λ_R), while the highest λ_R values correspond to S0 galaxies. Most SRs which are not 2σ galaxies are classified as Es (23/32).

As expected, the vast majority of galaxies with ellipticities $\epsilon_e > 0.5$ are S0s. However, 20 per cent of all FRs (45/224) are Es and 66 per cent of all Es in the ATLAS^{3D} sample are FRs. Also the fact that all 2σ galaxies except one (NGC 4473) are classified as S0s

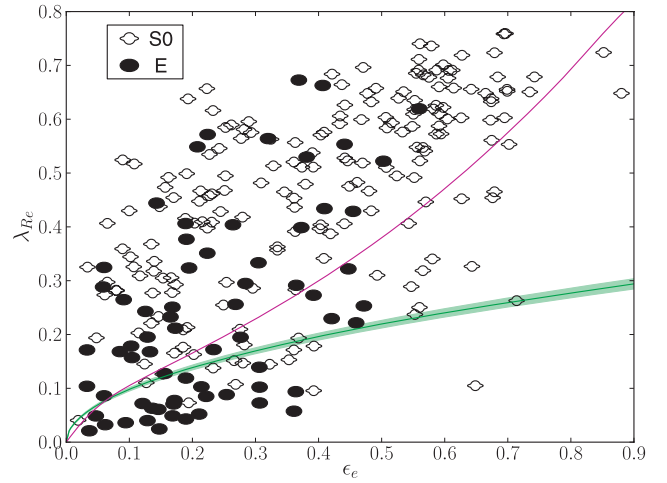


Figure 8. λ_R versus the ellipticity ϵ within an aperture of R_e . The lines are as in Fig. 7. The filled ellipses and open symbols are galaxies with a morphological type $T < -3.5$ (Es) and $T \geq -3.5$ (S0s), respectively. Note the Es which are FRs (above the green line).

demonstrates that the global morphology alone is not sufficient to reveal the dynamical state of ETGs. The E/S0 classification alone is obviously not a robust way to assess the dynamical state of a galaxy. There is in fact no clear correlation between $\lambda_R/\sqrt{\epsilon}$ and the morphological type T , besides the trends mentioned here. From Fig. 8, we expect a significant fraction of galaxies classified as Es to be inclined versions of systems which would be classified as S0s when edge-on, and just separating ETGs into Es and S0s is therefore misleading.

4.7 Properties of slow and fast rotators

The detailed distribution of galaxies in *groups a, b, c, d* and *e* as defined in Paper II is shown in Fig. 9 using histograms of $\lambda_R^N = \lambda_R/\sqrt{\epsilon}$ values both for R_e and $R_e/2$. The *group e* galaxies, and consequently the FRs, peak at a value of around 0.75 within $R_e/2$ and 0.85 for R_e . SRs are defined as galaxies with $\lambda_R^N < k_{FS}$, mostly associated with galaxies from *groups a* to *d*, which represent the lower tail of that distribution with some small overlap with *group e*. We provide the SAURON stellar velocity and velocity dispersion maps of all 36 SRs in Figs A1 and A2 of Appendix A. We refer the reader to Paper II for all other SAURON stellar velocity maps.

We re-emphasize in Figs 10 and 11 the trend for SRs to be on the high-mass end of our sample. SRs span the full range of dynamical masses present in the ATLAS^{3D} sample. However, most non-rotators and galaxies with KDCs have masses above $10^{10.75} M_\odot$. If we exclude the three potential face-on FRs (see Section 3), all non-rotators have masses above $10^{11.25} M_\odot$. These non-rotators and KDC galaxies clearly have a different mass distribution from 2σ galaxies which are all, except NGC 4473, below $10^{10.75} M_\odot$. The normalized λ_{Re}^N value for SRs tends to decrease with increasing mass (Fig. 10): the mean λ_{Re}^N values for SRs below and above a mass of $10^{11.25} M_\odot$ are about 0.22 and 0.13, respectively. FRs overall seem to be spread over all λ_{Re}^N values up to a dynamical mass $10^{11.25} M_\odot$ where we observe the most extreme instances of SRs (e.g. non-rotators). In Fig. 11, we show ϵ_e with respect to the dynamical mass M_{dyn} where we have coloured each symbol following the fast (blue) and slow (red) rotator classes. Fig. 11 also shows the fraction of SRs with respect to the total number of galaxies within certain mass bins: SRs represent between 5 and 15 per cent of all galaxies between 10^{10} and

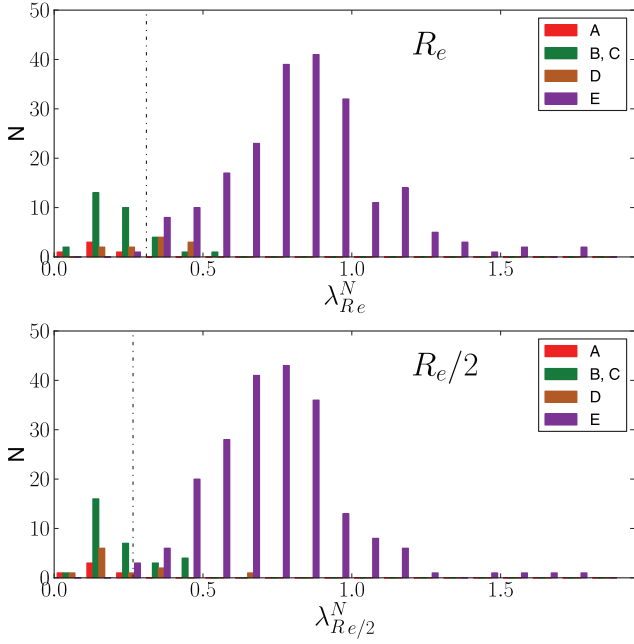


Figure 9. Histograms of galaxies in the ATLAS^{3D} sample showing the distribution of $\lambda_R^N = \lambda_R/\sqrt{\epsilon}$ within an aperture of $R_e/2$ (top panel) and R_e (bottom panel) for non-rotators (A), featureless non-regular rotators with or without a KDC (B and C) in green, 2σ galaxies (D) in orange and non-regular rotators (E) in purple. The vertical dashed lines in each panel show the limit set (0.265 and 0.31, for $R_e/2$ and R_e , respectively) between SRs and FRs for both apertures. To avoid confusion, we have excluded the two non-rotators, NGC 3703 and 4733, which are assumed to be face-on FRs.

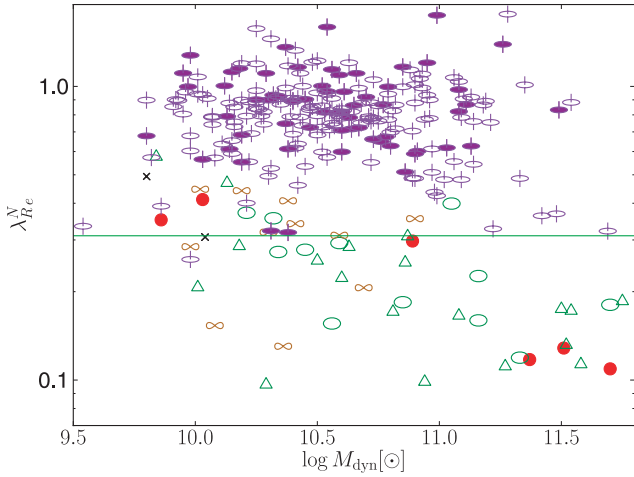


Figure 10. $\lambda_{R_e}^N$ (log-scale) versus dynamical masses M_{dyn} . Symbols are as in Fig. 7. The horizontal green solid line indicates the limit between FRs and SRs.

$10^{11.25} M_{\odot}$. As already mentioned, above $10^{11.25} M_{\odot}$ the fraction of SRs shoots up very significantly, reaching 45 and 77 per cent in the last two mass bins below and above $10^{11.5} M_{\odot}$, respectively.

There is a tendency for SRs above $10^{11} M_{\odot}$ to have rounder isophotes with ellipticities ϵ_e between 0 and 0.3 and mostly below 0.2, while most SRs below $10^{11} M_{\odot}$ have ellipticities distributed between 0.2 and 0.4 (Fig. 11). The weak trend for SRs at higher mass to have lower $\lambda_{R_e}^N$ could thus be associated with the corresponding ellipticity decrease. FRs seem to be smoothly distributed over the

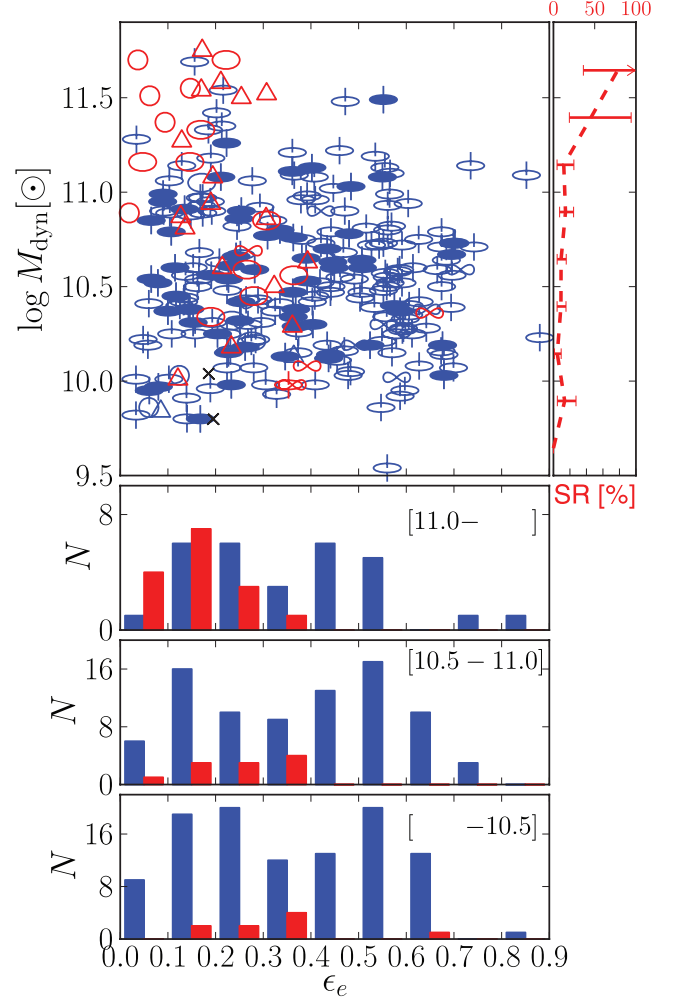


Figure 11. Dynamical masses M_{dyn} versus ϵ_e . The top left-hand panel shows the distribution of ATLAS^{3D} galaxies with the blue and red colours now correspond to FRs and SRs, respectively. Symbols are as in Fig. 7. The thick red dashed curve with error bars in the top right-hand panel shows the fraction of SRs (for $1R_e$) for mass bins with widths of 0.25 in $\log M_{\text{dyn}}$ with the corresponding labels given in the top x-axis. The three lower panels present the ellipticity within R_e histograms in bins of masses ($\log M_{\text{dyn}}$), indicated in brackets in each subpanel. Note the increased fraction of SRs in the two highest mass bins and the shift in the ellipticity of SRs above and below $10^{11} M_{\odot}$.

full range of ellipticities between $10^{9.75} M_{\odot}$, near the lower mass (luminosity) cut of our sample, and $10^{11.25} M_{\odot}$ above which SRs clearly dominate in numbers. All these results are also valid when using a smaller aperture ($R_e/2$).

4.8 Isophote shapes and central light profiles

Massive SRs have, as expected, slightly boxy isophotes, as shown in Fig. 12 where we present $\langle a_4 \rangle$, the luminosity-weighted average of a_4 within $1R_e$, versus the dynamical mass. This is a known result, specifically emphasized by Kormendy & Bender (1996) who suggested the use of the a_4 parameter, quantifying the degree of boxiness or disciness of the isophotes, to assess the dynamical status of ETGs. All nine galaxies within the ATLAS^{3D} sample with masses larger than $10^{11.5} M_{\odot}$ have a_4 values which are negative or very close to zero, but these include two FRs, namely NGC 3665 and

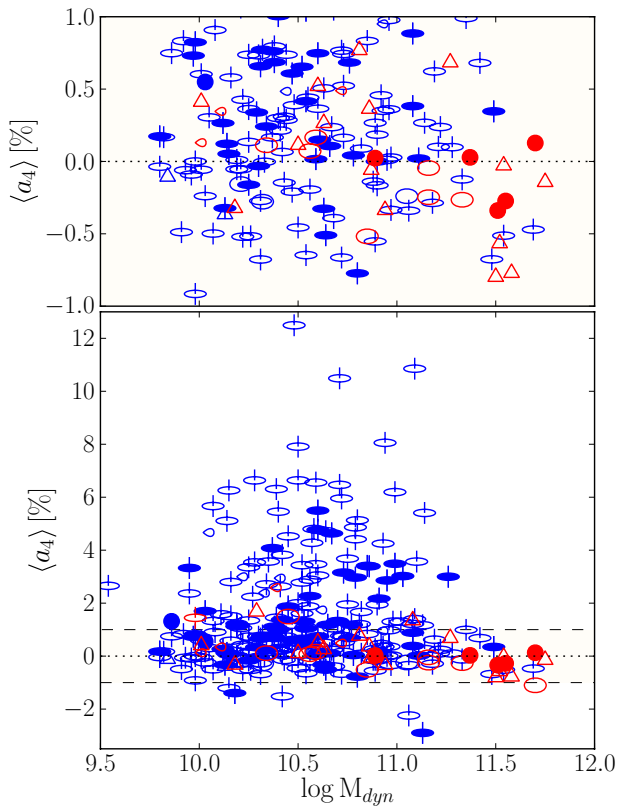


Figure 12. The averaged a_4 (in per cent within $1R_e$) versus the dynamical mass for galaxies in the ATLAS^{3D} sample. The top panel is a zoomed-in version of the bottom panel, including only a_4 values between -1 and $+1$. Symbols are as in the top panel of Fig. 11.

4649. In fact 70 per cent of the SRs more massive than $10^{11} M_\odot$ are boxy, while in the same mass range only 30 per cent of the FRs are boxy. Below a mass of $10^{11} M_\odot$, we observe the same overall fraction (~ 25 per cent) of boxy systems in both SRs and FRs. This means that the relative fraction of FRs which are boxy is nearly constant with mass, while there is a drastic change in the boxiness/disciness in the population of SRs around a mass of $10^{11} M_\odot$. We also note that most discy SRs exhibit a KDC or are 2σ galaxies. Since all 2σ galaxies are discy and the identification of such systems depends on the viewing angle, we should expect that some of these discy SRs are bona fide 2σ galaxies: a confirmation of this hypothesis requires detailed modelling of the photometry and stellar kinematics.

In Fig. 13, we now show how $\langle a_4 \rangle$ varies with the normalized value λ_{Re}^N with the symbols of the different kinemetry groups. Non-regular rotators with no specific kinematic feature (*group b*) are more often boxy. Galaxies with KDCs (*group c*) can be both discy or boxy. Larger positive disciness values are reached for higher λ_R values as already emphasized in E+07 and galaxies with $\langle a_4 \rangle$ larger than 3 per cent are all FRs. A little more than 20 per cent of all FRs are boxy (48/224), but most of them (32) have rather low absolute values (average boxiness of less than 0.5 per cent), and a few are boxy (e.g. NGC 3489 and 4233) because of the impact of dust on the isophote shapes. Among these boxy FRs, only 17 per cent are clearly barred (8/48): considering the size of that subsample, this is not significantly different from 28 per cent of FRs which are clearly barred (with this fraction of barred galaxies to be considered as a lower limit). Apart from the mass trend mentioned above, there

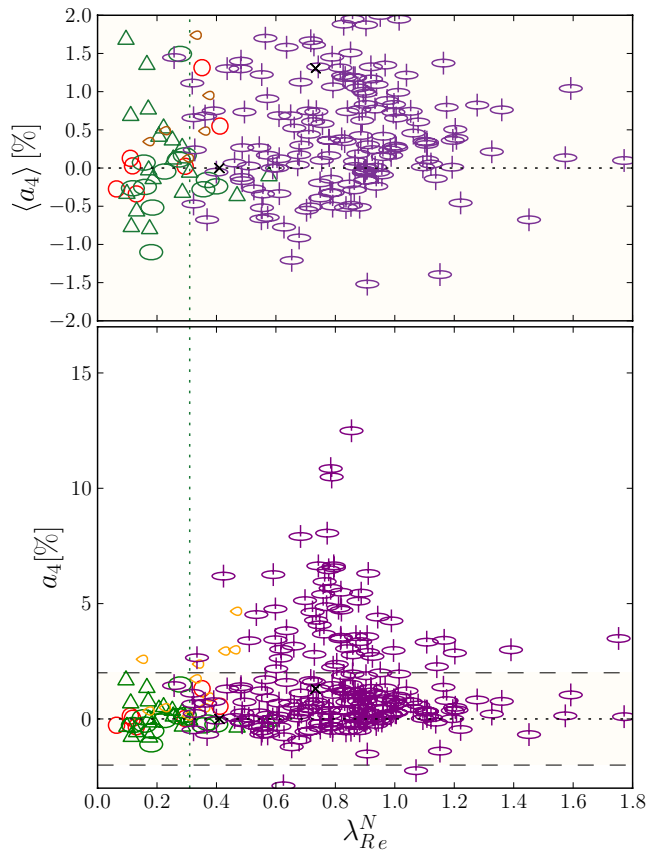


Figure 13. λ_{Re}^N versus the averaged a_4 (in per cent within $1R_e$). The top panel is a zoomed-in version of the bottom panel, including only a_4 values between -1 and $+1$. Symbols are as in Fig. 7. The vertical green dotted line represents the threshold between SRs and FRs, as defined in this paper.

seems to be no simple link between a_4 of galaxies in the ATLAS^{3D} sample and the SR and FR classes.

We also examine whether there is an existing link between the apparent stellar angular momentum measured via λ_R within $1R_e$ and the central light excess (or deficit): these central departures from simple photometric profiles (Sérsic laws) have been interpreted in various contexts, but the main processes which have been called upon are dissipational processes (gas filling in the central region and forming stars) to explain the light excesses and the black hole scouring (ejection of stars by binary black holes). In this context, Kormendy et al. (2009) have recently proposed that it represents an important tracer of the past history of the galaxy and suggested the existence of a dichotomy within the E class of galaxies (see also papers by Khochfar & Burkert 2005; Hopkins et al. 2009a,b,c). In Fig. 14, we present the central excess light value obtained by Kormendy et al. (2009, bottom panel) and Glass et al. (2011, top panel) in terms of the dynamical mass λ_{Re}^N (left-hand panels) and M_{dyn} (right-hand panels). We recover the trend already mentioned in Côté et al. (2007), Kormendy et al. (2009) and Glass et al. (2011) that central light excesses correlate with the luminosity (or mass). There is a clear trend for FRs to have central light excesses and for SRs to exhibit light deficits. The central light excess is, however, not strongly correlated with the distance to the threshold defining SRs and FRs; for example, FRs span a wide range of $\lambda_R/\sqrt{\epsilon}$ values irrespective of the measured central light excess. There is a remarkable exception in Fig. 14 for 2σ galaxies which are SRs but have light excesses: there, the morphology and photometry alone

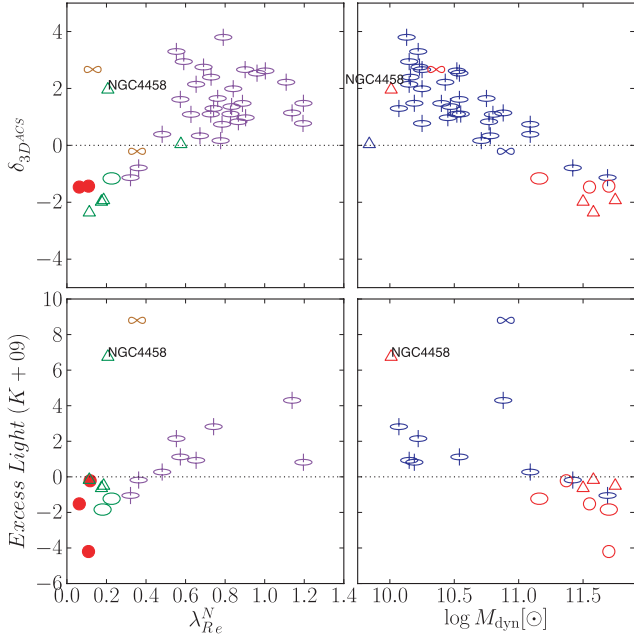


Figure 14. The central light deficit as derived by Glass et al. (2011, top panel) and Kormendy et al. (2009, bottom panel), for galaxies in common with the ATLAS^{3D} sample, versus λ_{Re}^N (left-hand panels) and the dynamical mass M_{dyn} (in log, right-hand panels). Symbols in the right-hand panels are as in Fig. 7, while in the left-hand panels, SRs are indicated as red symbols and FRs as blue symbols. NGC 4458 is emphasized as the only galaxy with a KDC (triangle) to have a positive value for the light excess.

fail to reveal the nature of the underlying stellar system, although there may exist associated photometric signatures. NGC 4458 also stands out as a SR, with a KDC (*group c*) and having a light excess which seems to correspond to a very central stellar disc (Morelli et al. 2004; Ferrarese et al. 2006). The existing trend between λ_R and the total luminosity or mass mentioned in this paper may be enough to explain the observed trend, for example, that SRs exhibit light deficits. However, the small number of objects in Fig. 14 is obviously a major concern in this context and we should wait for access to larger data sets before we can draw firm conclusions.

5 DISCUSSION

The results presented in the previous sections provide an updated view at ETGs in the nearby Universe, which we now briefly summarize before we further discuss the two *families* of FRs and SRs in turn, and mention how these families can relate to standard physical processes often *invoked* in the context of the galaxy formation and assembly.

The vast majority of ETGs in our sample are FRs: they dominate in numbers and represent nearly 70 per cent of the stellar mass in ETGs. **FRs are mostly discy galaxies** spanning a wide range of apparent ellipticities, the most flattened systems having ellipticities consistent with the ones of spiral galaxies. SRs represent only 15 per cent of all ETGs in the ATLAS^{3D} sample and dominate only the high-mass end of the ETG distribution. We witness three main types of SRs out of the 36 present in the ATLAS^{3D} sample:

(i) Non-rotating galaxies (four, excluding NGC 6703 which may be a face-on FR), which are all more massive than $10^{11.25} M_\odot$ and appear round, namely NGC 4374, 4486, 4436 and 5846;

(ii) Galaxies which cover a large range of masses (27), often with KDCs (18/27, including NGC 4476 in this set), and are never very flattened with ϵ_e smaller than 0.4. This includes seven galaxies which have KDCs observed as counter-rotating structures;

(iii) Lower-mass flattened 2σ galaxies (four), which are interpreted as including two large-scale stellar disc-like counter-rotating components.

The ATLAS^{3D} survey probes various galaxy environments and, obviously, the fraction of observed FRs and SRs would change with samples of galaxies biased towards, for example, higher galaxy densities (Cappellari et al. 2011b, hereafter Paper VII).

5.1 Fast rotators

We can now use our knowledge of the photometric and kinematic structures of FRs to predict roughly how a given sample of galaxies with particular properties would be distributed if viewed at random inclinations on the sky. A simple prescription could be applied to the family of FRs, as the vast majority of these exhibit regular stellar velocity maps consistent with the apparent disc-like rotation with no significant misalignments between the photometric and kinematic axes (see Paper II for more details on this specific issue). If the galaxies illustrated in Fig. 3, selected to be close to the $\beta = 0.65 \times \epsilon$ relation for oblate systems, are indeed viewed near edge-on, then FRs span quite a broad range of the intrinsic flattening within $1R_e$. In Fig. 3, the dashed lines emphasize the effect of the inclination for galaxies along this relation (see also Appendix B).

We therefore performed Monte Carlo simulations of a large sample of galaxies following a prescription similar to the one from C+07 (see also Appendix C). We take the distribution for the intrinsic ellipticities ϵ_{intr} of the simulated sample as a Gaussian centred at $\epsilon_0 = 0.7$ with a width $\sigma_\epsilon = 0.2$ for an aperture of $1R_e$. We fixed the β anisotropy distribution also as a Gaussian with a mean of $m_\beta = 0.5$ and a dispersion of $\sigma_\beta = 0.1$ truncated at $0.8 \times \epsilon_{intr}$ (see C+07). The result of the simulation (50 000 galaxies) is shown in Fig. 15 and it is qualitatively consistent with the distribution of FRs (see also a similar simulation, but for $R_e/2$ in Appendix B, Fig. B5). This tells us that in this context a reasonable approximation for such galaxies is a set of **oblate** systems with ellipticities peaking around 0.7, with most of the objects between 0.4 and 0.8. This confirms

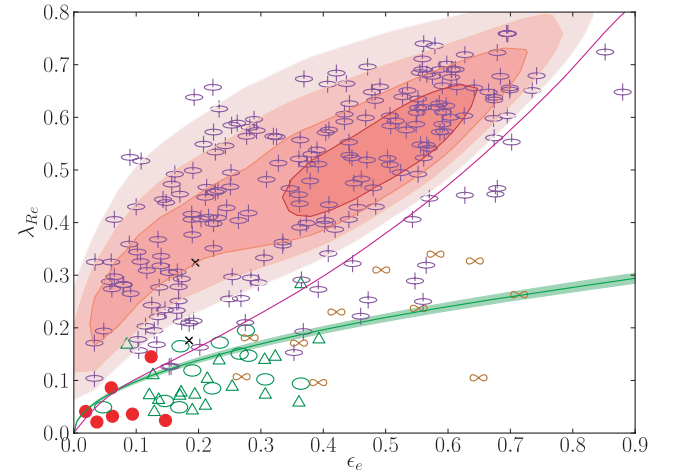


Figure 15. λ_{Re} versus the apparent ellipticity ϵ_e with flags indicating the observed kinematic structure with symbols as in Fig. 7. The coloured contours show the result of Monte Carlo realizations as described in the text. The green line shows the limit between SRs and FRs.

the visual impression provided in Fig. 3 illustrating the effect of the inclination (dashed lines). This Monte Carlo simulation also tells us that we should expect, from a sample of 224 FRs, an average of $\sim 4 \pm 2$ galaxies with λ_R below 0.1, which is consistent with our observed sample.

5.2 Slow rotators

Fig. 15 shows, as expected, that SRs are clearly inconsistent with the previously simulated data set. This confirms that the central regions of SRs are not similar to oblate systems, assuming some simple anisotropy–flattening relation as done in the previous section. Even an ellipticity distribution different from what was assumed in this simulation would not help to cover the region where SRs are located in a λ_R – ϵ diagram. Note that galaxies in *group d* have morphologies consistent with oblate systems but have unusually strong tangential anisotropies associated with the presence of two counter-rotating stellar discs. Observed misalignments between the kinematic and photometric axes in SRs also argue for these to be a different family of galaxies (Paper II) including non-axisymmetric and/or mildly triaxial systems.

As demonstrated by Jesseit et al. (2009) and confirmed in Paper V via numerical simulations of mergers, triaxial remnants which are SRs when viewed edge-on tend to appear as SRs (stay below the limiting line) for any projection. In the previous section, we have seen that there is only a low probability for a FR to be viewed (due to inclination effects) as a SR (something also emphasized by Jesseit et al. 2009) and here we suggest that **most galaxies appearing as SRs would still be SRs if viewed edge-on**. The only cases which are expected to potentially exhibit **ambiguous** classifications are **prolate** objects (Naab & Burkert 2003; Jesseit, Naab & Burkert 2005). We have two clear cases in our ATLAS^{3D} sample: NGC 4261 and 5485, the latter being classified as a FR here. NGC 5485 is a peculiar galaxy with its photometric major-axis being the symmetry axis for the dust lane and stellar rotation.

5.3 Early-type galaxy formation and assembly processes

Various physical processes often invoked for the formation and **assembly** of galaxies can contribute to or influence the specific angular momentum of the central stellar component of ETGs and consequently the measured λ_R value, and we briefly review these here in the context of the classification of ETGs into FRs and SRs.

Dissipative processes followed by the star formation should generally help preserve (or rebuild) stellar rotation in galaxies (see e.g. an early discussion in the context of ETGs in Bender, Burstein & Faber 1992). Accretion of gas from external sources, either via the large-scale filaments (e.g. Sancisi et al. 2008; Dekel et al. 2009; Khochfar & Silk 2009) or extracted by tidal forces from a gas-rich galaxy passing by, thus contributing to an **increase in λ_R if the gas is corotating with the main existing stellar component**, assuming that this additional gas forms stars. **This could also be a way for galaxies to rebuild a fast-rotating disc-like component**. Such a process should preferentially occur in gas-rich environments, for example, at high redshifts (z larger than about 2) and/or in low-density regions, disfavoured, for instance, the inner regions of dense clusters at moderate to low redshifts. An extreme version of such a mechanism is the case of very high gas fractions in disc-like objects, expected to be relevant mostly at high redshift: in such a situation, strong instabilities lead the galaxy to become **‘clumpy’**, with

massive gas clouds forming stars and evolving as a N -body system with low N (see e.g. Elmegreen, Bournaud & Elmegreen 2008; Elmegreen et al. 2009). Evolving in relative **isolation**, such a system can end up as a disc galaxy (a FR, e.g. Bournaud et al. 2008) where the contribution of its spheroidal component varies depending on the exact initial conditions (gas fraction, spatial distribution and angular momentum).

Subsequent evolution due to disc instabilities, spiral density waves and bars, will tend to heat the stellar component (Sellwood & Binney 2002; Debattista et al. 2006; Sales et al. 2009; Minchev & Famaey 2010) and decrease λ_R accordingly, but the global stellar angular momentum of FRs should not change dramatically because of such secular evolution processes. Such perturbations could, however, be a trigger for the inner gas fuelling then leading to the formation of a central rapidly rotating stellar component (e.g. Wozniak et al. 2003). Similarly, gas stripping from a galaxy, if done in a nearly adiabatic way, should not change λ_R too drastically, even though the system would morphologically and dynamically evolve on a relaxation time-scale and this may affect the morphology and dynamics of its central region. This should also concern the ram pressure stripping (Gunn & Gott 1972; Quilis, Moore & Bower 2000; Rasmussen, Ponman & Mulchaey 2006) or active galactic nucleus feedback if the major effect remains focused on the gas component.

For a disc-like (spiral) galaxy to become a SR, numerical simulations have suggested that it needs to accrete at least half of its stellar mass via mergers (Bournaud et al. 2007; Jesseit et al. 2009; Bois et al. 2010; Bois et al. 2011, hereinafter Paper VI). As the orbital angular momentum for a (binary) merger event is often the main contributor (Khochfar & Burkert 2006), major mergers can form FRs (Paper VI; see also Springel & Hernquist 2005) even from slowly rotating galaxy progenitors (Di Matteo et al. 2009), the outer structure being generally more significantly affected (Coccato et al. 2009). Numerical studies show anyway that, among binary mergers, only major 1:1 or 2:1 mergers can form SRs, as it requires enough baryonic angular momentum to be transferred outwards (see Paper VI for details). We illustrate this by indicating where the 1:1 and 2:1 major merger remnants (including the gas and star formation) conducted in Paper VII lie in a λ_R – ϵ diagram in Fig. 16, assuming that the progenitors were spiral galaxies which have λ_R values close to the maximum value observed for our sample of ETGs. There is a clear separation between the merger remnants which are SRs and FRs: this corresponds to an initially different sign of the spin of the more early type progenitor (Paper VI) with respect to the orbital angular momentum as illustrated by the red and blue areas (corresponding to retrograde and prograde spins, respectively) in Fig. 16. Although such a distinction may be damped if we more broadly sample the input parameters for the progenitors (including their mass ratios) or include more realistic merger trees, the criterion defined here to separate FRs and SRs seems to properly distinguish the two families of galaxies: the merger remnants in Paper VI, which are **FRs, all have regular velocity fields with small photometric versus kinematic misalignments**, while most of the remnants, which are SRs, have kpc-size KDCs (see also van den Bosch et al. 2008; Hoffman et al. 2010; Paper VI) and are spread over a wide range of misalignment angle values.

In a similar context, ‘ 2σ ’ galaxies (10 in our sample, four of which are SRs) clearly stand out in an ϵ –mass diagram within the SR class (see Fig. 11), and such systems could be formed when two spiral galaxies with (roughly) opposite spins merge (Crocker et al. 2009). Another **scenario** relies on the accretion of the external and counter-rotating gas in a spiral galaxy (Rubin et al. 1992). Crocker

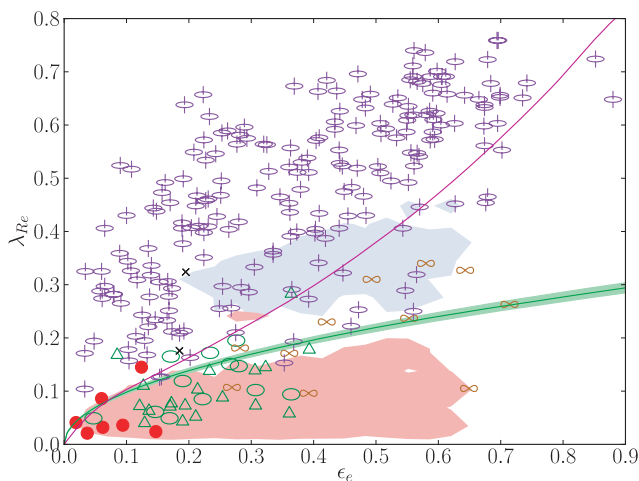


Figure 16. λ_{Re} versus the apparent ellipticity ϵ_e within $1R_e$ with symbols as in the bottom panel of Fig. 15. The blue- and red-coloured areas show the region where 1:1 and 2:1 merger remnants lie from the study of Paper VI: the red area corresponds to the merger remnants with a **retrograde** main progenitor (with respect to the orbital angular momentum), while the blue area corresponds to a prograde main progenitor. The green line shows the limit between SRs and FRs and the magenta line is as given in Fig. 7.

et al. (2009) recently suggested that the sense of rotation of the remnant gas component could indicate which scenario is preferred: associated with the **thicker** component for the merger scenario or with the thinner component for the accretion scenario. In the prototype galaxy NGC 4550, the gas rotates with the thicker stellar disc, favouring a merger event. However, other 2σ galaxies seem to show various configurations for the gas. We should also examine more cautiously a broader range of mergers forming such systems, as well as simulate the accretion of the counter-rotating gas, before we can go further and constrain the main formation process involved here. In any case, such SRs most probably require an existing cold, spiral-like progenitor and/or a gas-rich event (merger or accretion). The fact that such SRs show positive light excess (Fig. 14) contrary to other SRs is thus naturally explained if they formed and assembled via dissipative processes (accretion or merger), with the excess light being the consequence of a secondary star formation even in the central regions (Mihos & Hernquist 1994; Hopkins et al. 2009c; Kormendy et al. 2009).

To summarize, **ways to increase the central specific angular momentum of a galaxy are common, especially at high redshift, and often involve a gaseous dissipational process.** Among ETGs, FRs may therefore be expected to dominate in numbers at low redshifts, as long as the observed sample is not biased towards very dense environments (see Paper VII). The fastest early-type rotators should also be linked to their gas-richer counterpart, namely the spiral galaxies. Indeed, a galaxy like NGC4762 is an excellent illustration of a ‘dead’ spiral with a very high specific (stellar) angular momentum. Other FRs are the result of a complex history which certainly includes a mix of the processes mentioned in the present section and other potentially important ones, such as the stellar mass-loss (see e.g. Martig & Bournaud 2010).

SRs are the extreme instances of such a mixture of processes, where one of the most violent and disturbing mechanism, namely **major or repeated mergers**, disrupted their kinematical identity and for which there was little opportunity to transform back into a FR: this mostly happens either at the higher end of the mass function (e.g. Khochfar & Burkert 2006; Oser et al. 2010) or, specifically,

for low-mass galaxies which are the result of the merging of two counter-rotating (gaseous and/or stellar) components. This picture is consistent with the fact that **little or no molecular gas is found in SRs** (Young et al. 2011; Paper IV).

The detailed structure of nearby ETGs is a consequence of such a (non-exhaustive) list of processes: the exact distribution of ETGs in terms of a specific observable, for example, λ_R^N (Fig. 9), can then be simply interpreted as the convolution of the impact of each mechanism on that quantity with its relative contribution (this being obviously a naive view considering that each process does not act independently). We should therefore naturally expect a broad and continuous range in the properties of nearby ETGs. Since the relation defined to separate FRs and SRs is an empirical criterion, that is, based on observable quantities such as λ_R and ϵ , we should also expect a continuous range of properties among FRs linking them to the SRs, the final state of an individual galaxy depending on a given (complex) merging/accretion/evolution history. We indeed find galaxies near the dividing line with intermediate properties and there are a few misclassified systems. Still, the defined criterion for SRs and FRs operates rather well when the goal is to distinguish galaxies with complex central dynamical structures (e.g. large-scale stellar KDCs) from oblate systems with or without bars. We therefore suggest here that SRs are the extreme instances of such a mixture of processes where one of the most violent and disturbing mechanism, namely major or repeated mergers, disrupted their kinematical identity and for which there was little opportunity to transform back into a FR. This mostly happens either at the higher end of the mass function (e.g. Khochfar & Burkert 2006; Oser et al. 2010) or, specifically, for low-mass galaxies which are the result of the merging of two counter-rotating (gaseous and/or stellar) components. This picture is again consistent with the finding that **there seems to be little or no molecular gas in SRs** (Young et al. 2011; Paper IV). Most SRs have a mass above $10^{10.5} M_\odot$ and they clearly dominate the ETG population above $10^{11.25} M_\odot$. If the above-mentioned picture is correct, then the smoothness of the transition between a FR-dominated and a SR-dominated population of ETGs should directly depend on the availability of gas and the role of mergers. This is examined in detail in forthcoming papers, for example, in Khochfar et al. (2011) where semianalytic modelling techniques suggest that the amount of the accreted material and the ability to cool gas and make stars play a **prominent** role in this context. More specific studies of mergers are presented in Paper VI (numerical simulations of binary mergers) and more specifically presented in a cosmological context in Naab et al. (in preparation).

6 CONCLUSIONS

In this paper, we have used photometric and integral-field spectroscopic data to provide the first census of the apparent specific (stellar) angular momentum of a complete sample of 260 ETGs via the λ_R parameter.

We have shown that the apparent kinematic structures can be used to define a **refined** and **optimized** criterion to disentangle the so-called FRs and SRs. This new definition takes into account the fact that at a similar λ_R value, a more **flattened** galaxy is expected to exhibit a much stronger anisotropy. We are using a simple **proxy** with SRs being galaxies which have a specific stellar angular momentum within R_e as measured by λ_R less than 0.31 (0.265) times the square root of the ellipticity $\sqrt{\epsilon}$ measured within an aperture of $1R_e$ ($R_e/2$).

Using this relation, we find that 86 ± 2 per cent (224/260) of all ETGs in our ATLAS^{3D} sample are FRs. This result, associated with

the fact that FRs in the ATLAS^{3D} sample have aligned photometric and kinematic axes within 5° (Paper II), suggests that FRs are simple oblate systems (with or without bars) which span a range of intrinsic ellipticities between about 0.35 and 0.85. The remaining 14 per cent (36/260) of the ATLAS^{3D} sample are SRs: these are distributed between the well-known massive ($M > 10^{11} M_{\odot}$) and rather round ($\epsilon_e < 0.4$) galaxies (four being very massive non-rotators), often exhibiting central kinematically decoupled components, and a set of four (or 11 per cent of all SRs) lower mass objects ($M_{\text{dyn}} < 10^{10.5} M_{\odot}$) which exhibit two large-scale counter-rotating stellar disc systems (see Paper II for details).

We show that the suggested proxy, namely the a_4 parameter, is not efficient at distinguishing FRs from SRs. We also conclude that the separation of ETGs into the E and S0 classes is misleading. We do observe a trend, as expected, in the sense that most massive SRs are classified as Es and most FRs are classified as S0s. However, 66 per cent of all Es in our sample are FRs and, apart from a maximum ellipticity of 0.6, these are indistinguishable in our study from the rest of the FR population, a result already pointed out in E+07. We provide a quantitative and robust criterion to separate both families, via the λ_R parameter, while we expect only some small overlap around the defined threshold.

ETGs are the end-results of a complex set of formation and assembly processes, which shaped their morphology and dynamics. From the fastest rotating ETGs, which look like dead and red spirals, down to the slowest FRs, we observe no obvious discontinuity in their integrated properties. There is, however, a clear increase in the fraction of SRs above a mass of $\sim 10^{11.25} M_{\odot}$ (see Section 4.7), as well as above a certain local galaxy density (Paper VII). In this context, SRs represent the extreme instances of such red-sequence galaxies for which significant merging has occurred (sometimes with gas-rich systems but then at high redshift) and, being at the high end of the mass range of galaxies in the nearby Universe, do not get the opportunity to rebuild a cold stellar component from **dissipative** processes.

These results argue for a shift in the existing paradigm for ETGs, which are generally separated into disc-like S0 galaxies and spheroidal-like E systems. We find that the vast majority of ETGs in the nearby Universe are FRs (with 66 per cent of the Es in our sample being FRs), galaxies consistent with oblate systems with or without bars, while only a small fraction of them (less than 12 per cent), the tail of that distribution encompassing the most massive objects, have central (mildly) triaxial structures reflecting the more standard picture of an ellipsoidal (or spherical) stellar system.

ACKNOWLEDGMENTS

Part of this work has been conducted while visiting the Astronomy Department at the University of Texas at Austin under the auspices of a Beatrice Tinsley Scholarship. In this context, EE would like to warmly thank Neal Evans, Gordon Orris and John Kormendy for their hospitality. EE would also like to thank John Kormendy, Laura Ferrarese and Pat Côté for insightful discussions. EE thanks Lisa Glass and Pat Côté for sending an ASCII table with the δ_{3D} values published in Glass et al. (2011). This work was supported by the Agence Nationale de la Recherche under contract ANR-08-BLAN-0274-01. This work was supported by the rolling grants ‘Astrophysics at Oxford’ PP/E001114/1 and ST/H002456/1 and visitor grants PPA/V/S/2002/00553, PP/E001564/1 and ST/H504862/1 from the UK Research Councils. RLD acknowledges travel and computer grants from Christ Church, Oxford, and the support from the Royal Society in the form of a Wolfson Merit Award

502011.K502/jd. RLD also acknowledges the support of the ESO Visitor Programme which funded a 3-month stay in 2010. SK acknowledges support from the Royal Society Joint Projects Grant JP0869822. TN, SK and MB acknowledge support from the DFG Cluster of Excellence ‘Origin and Structure of the Universe’. MC acknowledges support from a STFC Advanced Fellowship (PP/D005574/1) and a Royal Society University Research Fellowship. MS acknowledges support from a STFC Advanced Fellowship ST/F009186/1. NS and TAD acknowledge support from an STFC studentship. RMMcD is supported by the Gemini Observatory, which is operated by the Association of Universities for Research in Astronomy, Inc., on behalf of the international Gemini partnership of Argentina, Australia, Brazil, Canada, Chile, the United Kingdom, and the United States of America. The authors acknowledge financial support from the ESO.



REFERENCES

- Abazajian K. N. et al., 2009, *ApJS*, 182, 543
 Bacon R. et al., 2001, *MNRAS*, 326, 23
 Bell E. F. et al., 2004, *ApJ*, 608, 752
 Bender R., 1988, *A&A*, 193, L7
 Bender R., Burstein D., Faber S. M., 1992, *ApJ*, 399, 462
 Bender R., Saglia R. P., Gerhard O. E., 1994, *MNRAS*, 269, 785
 Bernardi M., Shankar F., Hyde J. B., Mei S., Marulli F., Sheth R. K., 2010, *MNRAS*, 404, 2087
 Binney J., 2005, *MNRAS*, 363, 937
 Bois M. et al., 2010, *MNRAS*, 406, 2405
 Bois M. et al., 2011, *MNRAS*, submitted (Paper VI)
 Bournaud F., Jog C. J., Combes F., 2007, *A&A*, 476, 1179
 Bournaud F. et al., 2008, *A&A*, 486, 741
 Cappellari M., 2002, *MNRAS*, 333, 400
 Cappellari M., 2008, *MNRAS*, 390, 71
 Cappellari M., Copin Y., 2003, *MNRAS*, 342, 345
 Cappellari M., Emsellem E., 2004, *PASP*, 116, 138
 Cappellari M. et al., 2007, *MNRAS*, 379, 418 (C+07)
 Cappellari M. et al., 2010, *Highlights of Astronomy*, 15, 81
 Cappellari M. et al., 2011a, *MNRAS*, 413, 813 (Paper I)
 Cappellari M. et al., 2011b, *MNRAS*, in press, doi:10.1111/j.1365-2966.2011.18600.x (Paper VII)
 Coccato L. et al., 2009, *MNRAS*, 394, 1249
 Côté P. et al., 2006, *ApJS*, 165, 57
 Côté P. et al., 2007, *ApJ*, 671, 1456
 Crocker A. F., Jeong H., Komugi S., Combes F., Bureau M., Young L. M., Yi S., 2009, *MNRAS*, 393, 1255
 Davies R. L., Efsthathiou G., Fall S. M., Illingworth G., Schechter P. L., 1983, *ApJ*, 266, 41
 de Vaucouleurs G., de Vaucouleurs A., Corwin H. G., Jr, Buta R. J., Paturel G., Fouque P., 1991, *Third Reference Catalogue of Bright Galaxies*. Springer-Verlag, Berlin
 de Zeeuw P. T. et al., 2002, *MNRAS*, 329, 513
 Debattista V. P., Mayer L., Carollo C. M., Moore B., Wadsley J., Quinn T., 2006, *ApJ*, 645, 209
 Dekel A. et al., 2009, *Nat*, 457, 451
 Di Matteo P., Jog C. J., Lehnert M. D., Combes F., Semelin B., 2009, *A&A*, 501, L9
 Elmegreen B. G., Bournaud F., Elmegreen D. M., 2008, *ApJ*, 688, 67
 Elmegreen B. G., Elmegreen D. M., Fernandez M. X., Lemonias J. J., 2009, *ApJ*, 692, 12
 Emsellem E., Monnet G., Bacon R., 1994, *A&A*, 285, 723
 Emsellem E. et al., 2004, *MNRAS*, 352, 721
 Emsellem E. et al., 2007, *MNRAS*, 379, 401 (E+07)
 Ferrarese L. et al., 2006, *ApJS*, 164, 334
 Fukugita M. et al., 2007, *AJ*, 134, 579
 Geha M., Guhathakurta P., van der Marel R. P., 2005, *AJ*, 129, 2617

- Gerhard O. E., Jeske G., Saglia R. P., Bender R., 1999, in Barnes J. E., Sanders D. B., eds, *Proc. IAU Symp. 186, Galaxy Interactions at Low and High Redshift*. Kluwer, Dordrecht, p. 189
- Glass L. et al., 2011, *ApJ*, 726, 31
- Graham A. W., 2004, *ApJ*, 613, L33
- Graham A. W., Guzmán R., 2003, *AJ*, 125, 2936
- Gunn J. E., Gott J. R., III, 1972, *ApJ*, 176, 1
- Hoffman L., Cox T. J., Dutta S., Hernquist L., 2010, *ApJ*, 723, 818
- Hopkins P. F., Cox T. J., Dutta S. N., Hernquist L., Kormendy J., Lauer T. R., 2009a, *ApJS*, 181, 135
- Hopkins P. F., Hernquist L., Cox T. J., Keres D., Wuyts S., 2009b, *ApJ*, 691, 1424
- Hopkins P. F., Lauer T. R., Cox T. J., Hernquist L., Kormendy J., 2009c, *ApJS*, 181, 486
- Hubble E. P., 1936, *Realm of the Nebulae*. Yale University Press, New Haven
- Jarrett T. H., Chester R., Cutri R., Schneider S., Skrutskie M., Huchra J. P., 2000, *AJ*, 119, 2498
- Jesseit R., Naab T., Burkert A., 2005, *MNRAS*, 360, 1185
- Jesseit R., Cappellari M., Naab T., Emsellem E., Burkert A., 2009, *MNRAS*, 397, 1202
- Khochfar S., Burkert A., 2003, *ApJ*, 597, L117
- Khochfar S., Burkert A., 2005, *MNRAS*, 359, 1379
- Khochfar S., Burkert A., 2006, *A&A*, 445, 403
- Khochfar S., Silk J., 2009, *ApJ*, 700, L21
- Khochfar M. et al., 2011, *MNRAS*, submitted (Paper VIII)
- Kormendy J., Bender R., 1996, *ApJ*, 464, L119
- Kormendy J., Fisher D. B., Cornell M. E., Bender R., 2009, *ApJS*, 182, 216
- Krajnović D., Cappellari M., de Zeeuw P. T., Copin Y., 2006, *MNRAS*, 366, 787
- Krajnović D. et al., 2008, *MNRAS*, 390, 93
- Krajnović D. et al., 2011, *MNRAS*, in press (arXiv:1102.3801, doi:10.1111/j.1365-2966.2011.18560.x) (Paper II)
- Kriek M., van der Wel A., van Dokkum P. G., Franx M., Illingworth G. D., 2008, *ApJ*, 682, 896
- Li J. G., Seaquist E. R., 1994, *AJ*, 107, 1953
- McIntosh D. H. et al., 2005, *ApJ*, 632, 191
- Martig M., Bournaud F., 2010, *ApJ*, 714, L275
- Mihos J. C., Hernquist L., 1994, *ApJ*, 437, L47
- Minchev I., Famaey B., 2010, *ApJ*, 722, 112
- Morelli L. et al., 2004, *MNRAS*, 354, 753
- Naab T., Burkert A., 2001, *ApJ*, 555, L91
- Naab T., Burkert A., 2003, *ApJ*, 597, 893
- Naab T., Burkert A., Hernquist L., 1999, *ApJ*, 523, L133
- Naab T., Johansson P. H., Ostriker J. P., Efstathiou G., 2007, *ApJ*, 658, 710
- Naab T., Johansson P. H., Ostriker J. P., 2009, *ApJ*, 699, L178
- Oser L., Ostriker J. P., Naab T., Johansson P. H., Burkert A., 2010, *ApJ*, 725, 2312
- Paturel G., Petit C., Prugniel P., Theureau G., Rousseau J., Brouty M., Dubois P., Cambrélys L., 2003, *A&A*, 412, 45
- Quilis V., Moore B., Bower R., 2000, *Sci*, 288, 1617
- Rasmussen J., Ponman T. J., Mulchaey J. S., 2006, *MNRAS*, 370, 453
- Rix H.-W., White S. D. M., 1990, *ApJ*, 362, 52
- Rix H.-W., Franx M., Fisher D., Illingworth G., 1992, *ApJ*, 400, L5
- Rix H.-W., Carollo C. M., Freeman K., 1999, *ApJ*, 513, L25
- Rubin V. C., Graham J. A., Kenney J. D. P., 1992, *ApJ*, 394, L9
- Sales L. V. et al., 2009, *MNRAS*, 400, L61
- Sánchez-Blázquez P. et al., 2006, *MNRAS*, 371, 703
- Sancisi R., Fraternali R., Oosterloo T., van der Hulst T., 2008, *A&AR*, 15, 189
- Scorza C., van den Bosch F. C., 1998, *MNRAS*, 300, 469
- Scott N. et al., 2009, *MNRAS*, 398, 1835
- Sellwood J. A., Binney J. J., 2002, *MNRAS*, 336, 785
- Springel V., Hernquist L., 2005, *ApJ*, 622, L9
- van den Bosch R. C. E., van de Ven G., Verolme E. K., Cappellari M., de Zeeuw P. T., 2008, *MNRAS*, 385, 647
- Wozniak H., Combes F., Emsellem E., Friedli D., 2003, *A&A*, 409, 469
- Young L. et al., 2011, *MNRAS* (arXiv:1102.4633, doi:10.1111/j.1365-2966.2011.18561.x) (Paper IV)

APPENDIX A: STELLAR VELOCITY AND DISPERSION MAPS OF SLOW ROTATORS IN THE ATLAS^{3D} SAMPLE

We provide here two figures (Figs A1 and A2) illustrating the stellar velocity and dispersion maps for the 36 SRs of our ATLAS^{3D} sample. Galaxies are sorted by (increasing) mass from the left-hand to right-hand side (top to bottom).

Fig. A1 emphasizes the non-regularity of the velocity fields of SRs, as well as the presence of large-scale (kpc-size) KDCs. It also illustrates that the galaxies with the zero apparent rotation (NGC 4374, 4486 and 5846) are among the most massive SRs. The dispersion maps provided in Fig. A2 illustrate, for example, how the stellar velocity dispersion peaks along the major-axis away from the centre for the SRs which were labelled ‘double σ ’ in Krajnović et al. (2011): these systems (e.g. NGC 4550 and 4528) are on the low-mass end of our sample.

APPENDIX B: DYNAMICAL MODELS, V/σ AND λ_R

In E+07 (see their appendix B), it has been shown that a tight relation exists between λ_R and V/σ for simple two-integral Jeans models, namely

$$\lambda_R = \frac{\langle RV \rangle}{\langle R\sqrt{V^2 + \sigma^2} \rangle} \approx \frac{\kappa (V/\sigma)}{\sqrt{1 + \kappa^2 (V/\sigma)^2}}. \quad (\text{B1})$$

The value of κ was estimated both from observations and from models to be ~ 1.1 .

Here we wish to extend this work both for our complete ATLAS^{3D} sample and for additional models. We have now derived a series of dynamical models for ellipsoidal or spheroidal systems with various intrinsic flattening (with ellipticities from 0 to 0.9), luminosity (or mass) profiles (Sérsic profiles with $n = 2$ or 4) and anisotropy parameters (β from 0 to 0.6). The dynamical models have an axisymmetric mass distribution described by the MGE parametrization (Emsellem et al. 1994), which was derived by fitting a one-dimensional Sérsic profile with the MGE routines of Cappellari (2002). The models assume a spatially-constant, cylindrically aligned and oblate ($\sigma_\phi = \sigma_R$) velocity ellipsoid (where σ_ϕ and σ_R are the azimuthal and radial velocity dispersion, respectively) characterized by the anisotropy parameter $\beta = 1 - (\sigma_z/\sigma_R)^2$. Under these assumptions, the unique prediction for the two-dimensional V and σ fields for the models was computed by solving the anisotropic Jeans equations with the routines of Cappellari (2008). The two-dimensional kinematics of the models were projected at different inclinations and were integrated within elliptical apertures of effective radii R_e or $R_e/2$, in the same way as for the observed systems.

We first confirm that $\kappa = 1.1$ for equation (B1) provides a good fit for both the models and our complete ATLAS^{3D} sample (see Fig. B1), although the slope is slightly steeper for the observed galaxies than for the models (see also Fig. B2), and the optimal value does in fact vary significantly depending on the inclination and anisotropy. We present the predictions of these models for λ_R versus ϵ for anisotropy β values from 0 to 0.6 in Fig. B3 and for apertures of $1R_e$ and $R_e/2$ in Fig. B4. Assuming a relation of the form given in equation (B1) holds between V/σ and λ_R , we can translate any relation such as $(V/\sigma)(x_1) = C(V/\sigma)(x_2)$ by $f_{\lambda_R}(x_1) = C f_{\lambda_R}(x_2)$, where

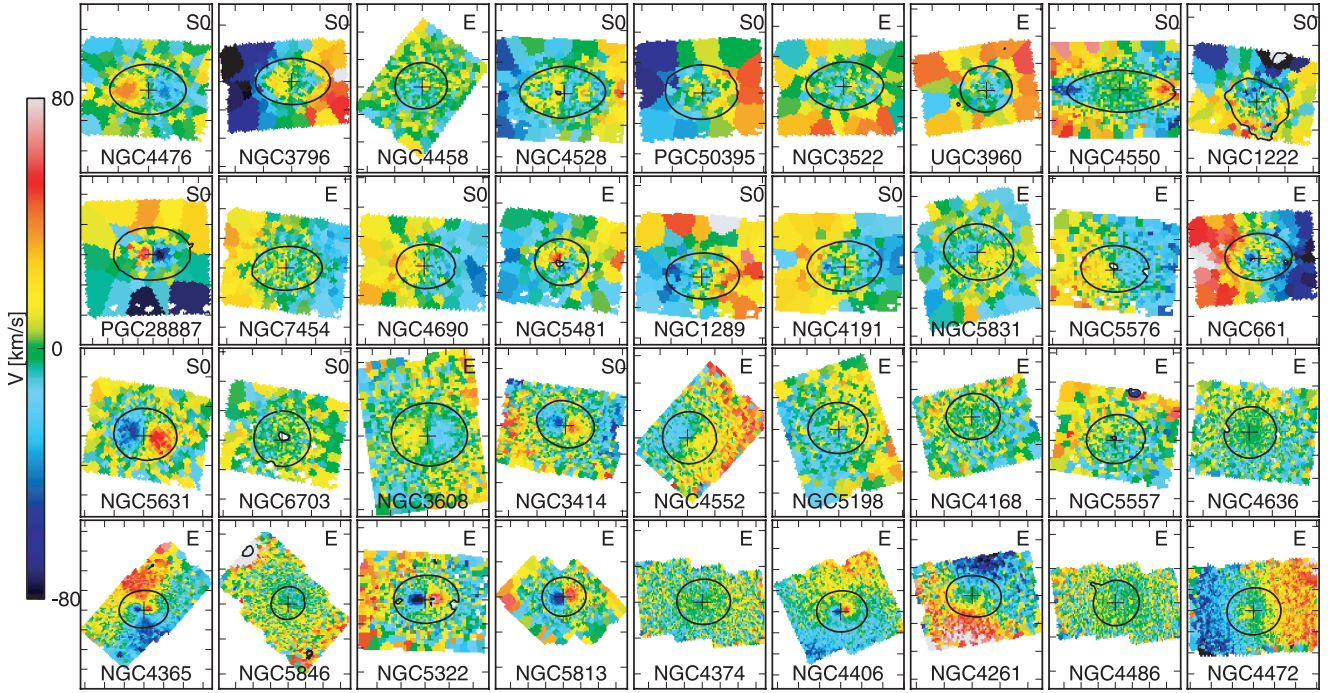


Figure A1. Stellar velocity fields for the 36 early-type SRs in the ATLAS^{3D} sample. We used the outer photometric axis to align all galaxies horizontally. Colour cuts have been adapted to each individual map. The solid black contour corresponds to a representative isophote and the centre of the galaxy is indicated by a cross. From the top to bottom (left-hand to right-hand side) the order follows the (increasing) dynamical mass values. The names of the galaxies and their Hubble types (E or S0) are also indicated. The colour cuts have been set up to ± 80 (km s^{-1}) for all maps.

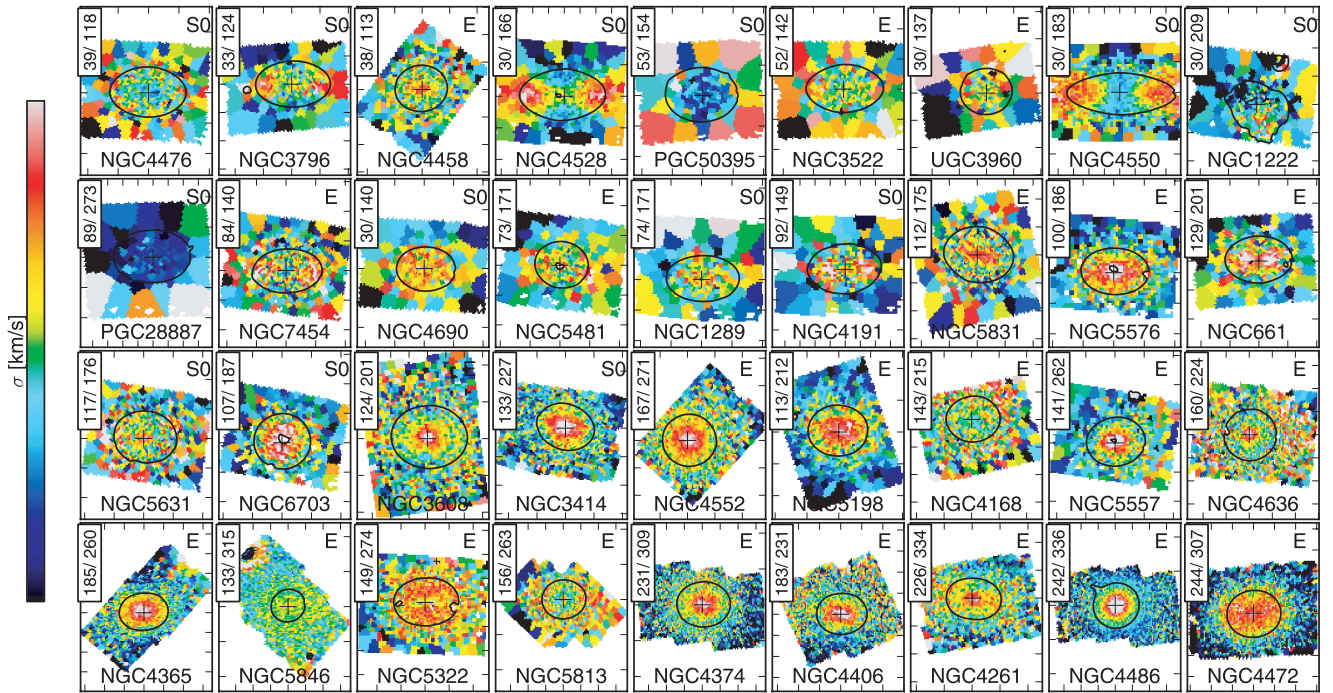


Figure A2. Stellar velocity dispersion fields for the 36 early-type SRs in the ATLAS^{3D} sample. See Fig. A1 for details. The specific colour cuts adapted to each dispersion map are specified in each inset (in km s^{-1}).

$f_{\lambda_R} = \lambda_R / \sqrt{1 - \lambda_R^2}$. We find that generally $(V/\sigma)_e \sim 1.1$ $(V/\sigma)_{e/2}$ and accordingly that $f_{\lambda_R}(R_e) \sim 1.15 f_{\lambda_R}(R_e/2)$: the constant of proportionality slightly changes from 1.1 to 1.15 here mainly because κ in equation (B1) is not exactly constant as we go to smaller apertures.

We then provide the best-fitting relations for λ_R and V/σ as functions of the ellipticity ϵ for isotropic systems, as given by $k_1 \sqrt{\frac{\epsilon}{1 - k_2 \epsilon}}$. The theoretical values for k_1 and k_2 are 0.831 and 0.896, respectively, using the entire dynamical system and assuming $\alpha = 0.15$ (see Binney 2005). This corresponds to values of $k_1 \sim 0.90$ and

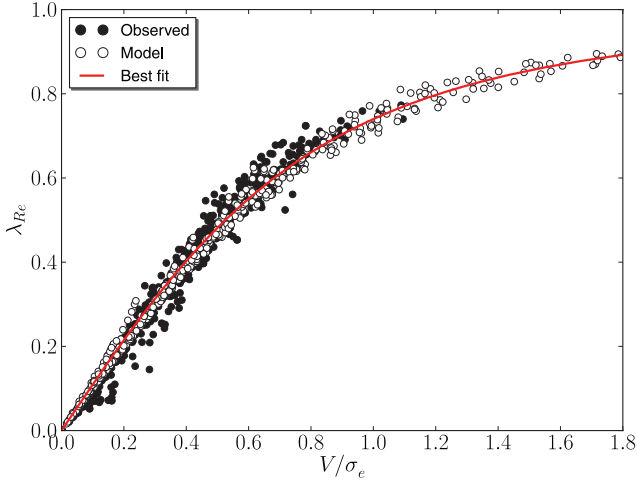


Figure B1. λ_R versus V/σ from the relation given in equation (B1). Results from the dynamical models are shown as the open circles and measurements resulting from the ATLAS^{3D} observations are shown as the black circles. The solid red line is the best-fitting relation following equation (B1) with $\kappa = 1.1$. Note that the observations exhibit a slightly steeper slope.

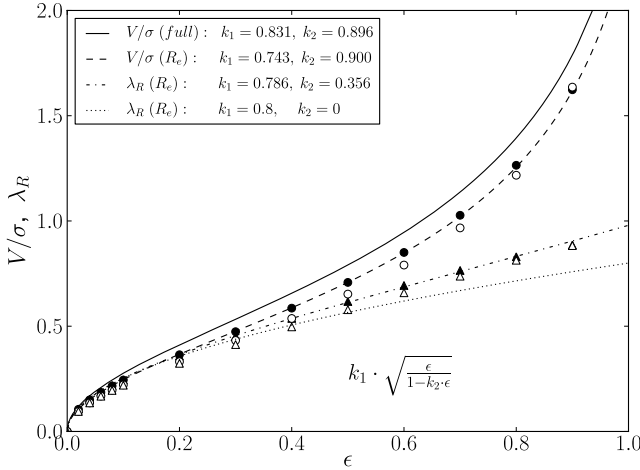


Figure B2. λ_R (triangles) and V/σ (circles) as functions of the ellipticity ϵ for isotropic systems: the expected theoretical formula is shown as a solid line (with $\alpha = 0.15$, see Binney 2005, for details and notations), while the dashed and dot-dashed lines provide the best fits to the edge-on values for V/σ and λ_R derived within $1R_e$, respectively. The filled and open symbols are for mass profiles with the Sérsic indices $n = 4$ and 2 , respectively. The dotted line shows the approximation using a simple law where $\lambda_R \propto \sqrt{\epsilon}$.

$k_2 \sim 0.08$ for λ_R . This means that λ_R is nearly proportional to $\sqrt{\epsilon}$ for isotropic systems (with $\alpha = 0.15$), leading to a reasonable approximation for low values of the ellipticity with $\lambda_R \sim 0.91 \times \sqrt{\epsilon}$ and a best-fitting approximation over a range $[0-0.9]$ of ellipticities given by $0.93\sqrt{\epsilon}$. As shown in C+07, the expected values using an effective aperture of $R_e/2$ are slightly smaller but would be close to the theoretical values obtained with $\alpha \sim 0.2$. The best-fitting relation for edge-on values within $1R_e$ gives $k_1 = 0.743$ and $k_2 = 0.900$ for V/σ . There is a slight dependency of these parameters when the mass profile is changed (Sérsic index $n = 4$ and 2), as expected.

The corresponding (edge-on) best-fitting relation for λ_R provides $k_1 = 0.786$ and $k_2 = 0.355$ for apertures of $1R_e$, and $k_1 = 0.69$ and $k_2 = 0.50$ for $R_e/2$. Restricting ourselves to the lower range of ellipticities (below 0.35), we have $\lambda_R \sim 0.8 \times \sqrt{\epsilon}$ and $\lambda_R \sim 0.71 \times \sqrt{\epsilon}$ for apertures of $1R_e$ and $R_e/2$, respectively.

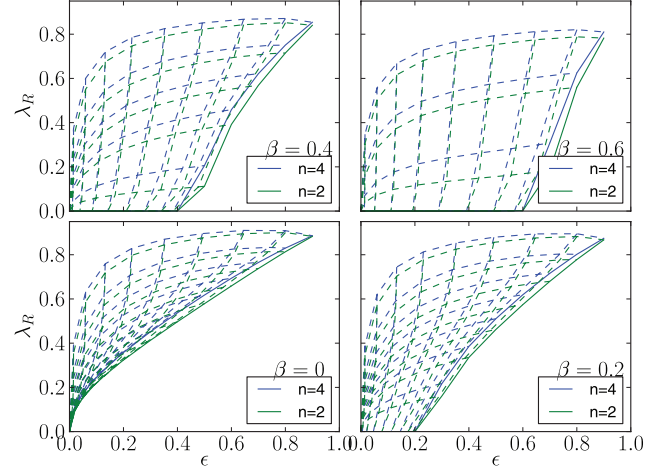


Figure B3. λ_R versus the ellipticity ϵ for different values of the anisotropy parameter β and two Sérsic profiles ($n = 2$ and 4).

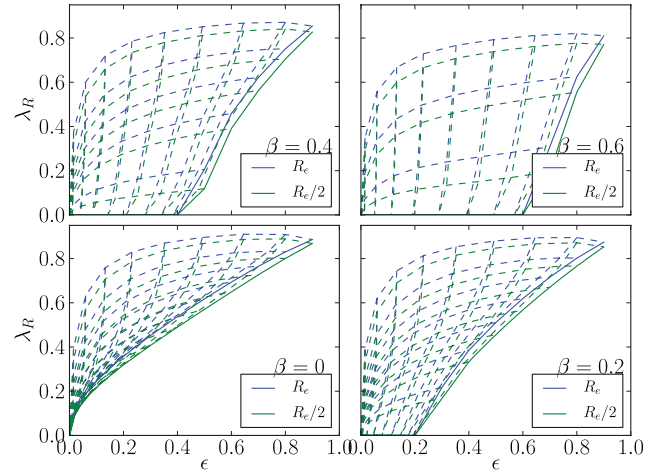


Figure B4. λ_R versus the ellipticity ϵ for apertures of $1R_e$ and $R_e/2$.

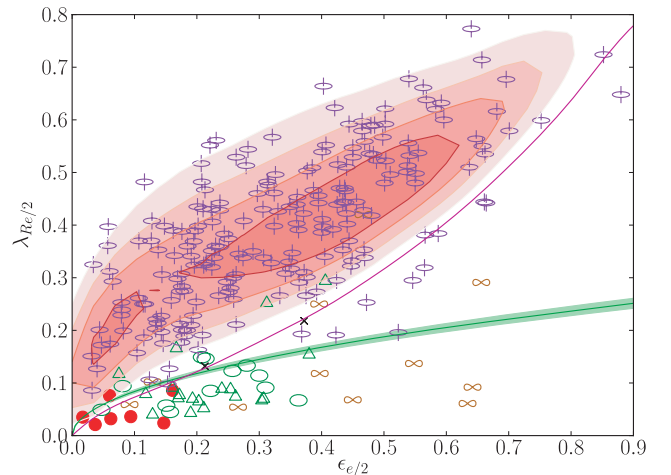


Figure B5. $\lambda_{R_e/2}$ versus the apparent ellipticity $\epsilon_{e/2}$ with flags indicating the observed kinematic structure with symbols as in Fig. 7. The coloured contours show the result of a Monte Carlo realization as described in the text. The green line shows the limit between SRs and FRs.

Table B1. Ellipticities, λ_R and V/σ tabulated values for the ATLAS^{3D} sample or 260 ETGs.

Name	R_{\max}	ϵ_e	$\epsilon_e/2$	Band (ϵ)	V/σ_e	$V/\sigma_e/2$	λ_{Re}	$\lambda_{Re}/2$	F/S (R_e)	F/S ($R_e/2$)
(1)	(2)	(3)	(4)	(5)	(6)	(7)	(8)	(9)	(10)	(11)
IC 0560	1.10	0.587	0.479	G	0.770	0.607	0.691	0.589	F	F
IC 0598	1.39	0.579	0.502	G	0.896	0.629	0.736	0.592	F	F
IC 0676	0.68	0.524	0.664	G	0.508	0.436	0.495	0.442	F	F
IC 0719	1.06	0.714	0.642	R	0.279	0.117	0.263	0.092	F	S
IC 0782	0.76	0.404	0.263	G	0.677	0.608	0.571	0.529	F	F
IC 1024	1.18	0.679	0.752	G	0.916	0.647	0.724	0.599	F	F
IC 3631	1.11	0.560	0.524	G	0.218	0.173	0.250	0.196	F	F
NGC 0448	1.22	0.643	0.656	G	0.380	0.377	0.327	0.291	F	F
NGC 0474	0.52	0.192	0.191	G	0.229	0.227	0.213	0.210	F	F
NGC 0502	1.44	0.146	0.047	G	0.213	0.168	0.234	0.172	F	F
NGC 0509	0.56	0.679	0.661	G	0.451	0.430	0.465	0.444	F	F
NGC 0516	0.95	0.699	0.701	G	0.786	0.624	0.655	0.579	F	F
NGC 0524	0.50	0.034	0.034	G	0.344	0.344	0.325	0.325	F	F
NGC 0525	1.41	0.280	0.173	G	0.404	0.285	0.418	0.274	F	F
NGC 0661	1.33	0.306	0.307	G	0.134	0.094	0.139	0.070	S	S
NGC 0680	1.19	0.189	0.185	G	0.413	0.361	0.406	0.360	F	F
NGC 0770	2.01	0.276	0.299	G	0.184	0.117	0.195	0.114	F	S
NGC 0821	0.49	0.392	0.392	G	0.288	0.288	0.273	0.273	F	F
NGC 0936	1.00	0.223	0.223	C	0.677	0.448	0.657	0.430	F	F
NGC 1023	0.47	0.363	0.363	G	0.372	0.372	0.391	0.391	F	F
NGC 1121	2.14	0.559	0.450	G	0.828	0.587	0.711	0.548	F	F
NGC 1222	1.12	0.280	0.280	C	0.153	0.138	0.147	0.132	S	S
NGC 1248	1.10	0.227	0.138	G	0.521	0.337	0.535	0.353	F	F
NGC 1266	0.88	0.193	0.207	G	0.775	0.589	0.638	0.517	F	F
NGC 1289	0.90	0.393	0.380	G	0.172	0.154	0.178	0.154	S	S
NGC 1665	0.65	0.491	0.440	G	0.669	0.478	0.658	0.511	F	F
NGC 2481	1.26	0.684	0.467	G	0.686	0.399	0.678	0.428	F	F
NGC 2549	0.88	0.587	0.488	G	0.623	0.563	0.572	0.523	F	F
NGC 2577	1.13	0.471	0.421	G	0.874	0.733	0.696	0.623	F	F
NGC 2592	1.39	0.208	0.210	G	0.529	0.422	0.549	0.431	F	F
NGC 2594	2.92	0.403	0.433	G	0.455	0.450	0.404	0.444	F	F
NGC 2679	0.46	0.368	0.368	G	0.185	0.185	0.193	0.193	F	F
NGC 2685	0.90	0.612	0.592	G	0.840	0.734	0.691	0.632	F	F
NGC 2695	1.04	0.293	0.225	G	0.582	0.422	0.575	0.406	F	F
NGC 2698	1.27	0.516	0.267	S	0.569	0.331	0.593	0.345	F	F
NGC 2699	1.39	0.143	0.202	G	0.450	0.393	0.444	0.398	F	F
NGC 2764	1.25	0.614	0.662	G	0.783	0.568	0.658	0.535	F	F
NGC 2768	0.35	0.472	0.472	G	0.236	0.236	0.253	0.253	F	F
NGC 2778	1.05	0.224	0.201	G	0.574	0.419	0.572	0.435	F	F
NGC 2824	2.49	0.162	0.107	G	0.534	0.407	0.492	0.370	F	F
NGC 2852	2.60	0.135	0.043	G	0.320	0.186	0.368	0.201	F	F
NGC 2859	0.60	0.089	0.057	G	0.410	0.408	0.359	0.361	F	F
NGC 2880	0.81	0.282	0.208	G	0.627	0.508	0.581	0.482	F	F
NGC 2950	1.11	0.362	0.237	G	0.488	0.472	0.436	0.428	F	F
NGC 2962	0.64	0.484	0.319	G	0.376	0.298	0.430	0.329	F	F
NGC 2974	0.53	0.407	0.403	R	0.813	0.811	0.663	0.664	F	F
NGC 3032	1.32	0.102	0.176	G	0.267	0.173	0.344	0.201	F	F
NGC 3073	1.24	0.124	0.162	G	0.136	0.092	0.145	0.086	F	S
NGC 3098	1.20	0.553	0.440	S	0.744	0.446	0.635	0.422	F	F
NGC 3156	0.96	0.478	0.469	G	0.771	0.611	0.648	0.559	F	F
NGC 3182	0.79	0.166	0.195	G	0.372	0.405	0.306	0.369	F	F
NGC 3193	0.57	0.129	0.143	G	0.208	0.208	0.195	0.197	F	F
NGC 3226	0.53	0.168	0.159	G	0.273	0.275	0.251	0.257	F	F
NGC 3230	0.81	0.550	0.360	G	0.617	0.393	0.609	0.403	F	F
NGC 3245	0.62	0.442	0.444	G	0.624	0.579	0.626	0.592	F	F
NGC 3248	1.09	0.374	0.290	G	0.514	0.380	0.511	0.350	F	F
NGC 3301	0.81	0.507	0.324	G	0.676	0.550	0.603	0.461	F	F
NGC 3377	0.42	0.503	0.503	G	0.564	0.564	0.522	0.522	F	F
NGC 3379	0.50	0.104	0.104	G	0.152	0.152	0.157	0.157	F	F
NGC 3384	0.54	0.065	0.058	G	0.456	0.449	0.407	0.397	F	F
NGC 3400	1.02	0.437	0.437	C	0.764	0.480	0.664	0.470	F	F

Table B1 – continued

Name	R_{\max}	ϵ_e	$\epsilon_e/2$	Band (ϵ)	V/σ_e	$V/\sigma_{e/2}$	λ_{Re}	$\lambda_{Re}/2$	F/S (R_e)	F/S ($R_e/2$)
(1)	(2)	(3)	(4)	(5)	(6)	(7)	(8)	(9)	(10)	(11)
NGC 3412	0.51	0.441	0.441	C	0.375	0.371	0.406	0.403	F	F
NGC 3414	0.67	0.194	0.193	G	0.106	0.107	0.073	0.070	S	S
NGC 3457	1.28	0.033	0.032	S	0.109	0.091	0.104	0.086	F	F
NGC 3458	1.61	0.231	0.114	G	0.438	0.245	0.461	0.250	F	F
NGC 3489	0.77	0.262	0.221	G	0.687	0.621	0.589	0.552	F	F
NGC 3499	2.03	0.139	0.143	G	0.323	0.236	0.318	0.227	F	F
NGC 3522	1.75	0.361	0.262	S	0.080	0.091	0.058	0.074	S	S
NGC 3530	1.91	0.642	0.555	G	0.741	0.554	0.656	0.537	F	F
NGC 3595	1.10	0.507	0.376	G	0.456	0.278	0.510	0.301	F	F
NGC 3599	0.65	0.080	0.080	C	0.273	0.241	0.282	0.239	F	F
NGC 3605	0.95	0.409	0.353	R	0.415	0.336	0.434	0.347	F	F
NGC 3607	0.60	0.185	0.194	G	0.283	0.294	0.209	0.228	F	F
NGC 3608	0.49	0.190	0.190	G	0.054	0.054	0.043	0.043	S	S
NGC 3610	1.10	0.381	0.400	G	0.642	0.639	0.530	0.539	F	F
NGC 3613	0.59	0.460	0.423	G	0.202	0.176	0.222	0.191	F	F
NGC 3619	0.62	0.173	0.176	G	0.285	0.274	0.293	0.283	F	F
NGC 3626	0.57	0.591	0.583	G	0.728	0.681	0.660	0.620	F	F
NGC 3630	1.04	0.665	0.371	G	0.639	0.404	0.648	0.421	F	F
NGC 3640	0.76	0.191	0.224	G	0.370	0.315	0.377	0.320	F	F
NGC 3641	1.84	0.125	0.215	G	0.331	0.353	0.243	0.328	F	F
NGC 3648	1.24	0.421	0.326	G	0.711	0.479	0.684	0.496	F	F
NGC 3658	0.91	0.243	0.148	G	0.462	0.336	0.546	0.398	F	F
NGC 3665	0.77	0.216	0.176	G	0.463	0.439	0.410	0.388	F	F
NGC 3674	1.28	0.568	0.342	G	0.491	0.292	0.541	0.308	F	F
NGC 3694	1.71	0.268	0.208	G	0.269	0.203	0.256	0.191	F	F
NGC 3757	2.06	0.153	0.153	C	0.119	0.096	0.126	0.098	F	S
NGC 3796	1.53	0.361	0.398	G	0.164	0.111	0.171	0.119	S	S
NGC 3838	1.42	0.605	0.385	S	0.743	0.536	0.676	0.509	F	F
NGC 3941	0.66	0.251	0.251	C	0.439	0.352	0.468	0.373	F	F
NGC 3945	0.74	0.090	0.230	G	0.717	0.741	0.524	0.561	F	F
NGC 3998	0.87	0.170	0.164	G	0.415	0.326	0.454	0.342	F	F
NGC 4026	0.75	0.556	0.438	G	0.540	0.451	0.548	0.442	F	F
NGC 4036	0.53	0.555	0.540	G	0.818	0.803	0.685	0.678	F	F
NGC 4078	2.00	0.561	0.510	S	0.575	0.524	0.523	0.496	F	F
NGC 4111	1.25	0.582	0.498	S	0.720	0.663	0.619	0.567	F	F
NGC 4119	0.61	0.598	0.563	G	0.895	0.808	0.701	0.660	F	F
NGC 4143	0.73	0.390	0.324	G	0.504	0.369	0.538	0.398	F	F
NGC 4150	0.98	0.328	0.274	G	0.514	0.337	0.513	0.338	F	F
NGC 4168	0.46	0.129	0.129	G	0.047	0.047	0.040	0.040	S	S
NGC 4179	0.77	0.591	0.501	G	0.589	0.470	0.587	0.480	F	F
NGC 4191	1.54	0.269	0.092	G	0.105	0.073	0.107	0.059	S	S
NGC 4203	0.59	0.154	0.180	G	0.281	0.255	0.305	0.275	F	F
NGC 4215	0.83	0.702	0.444	G	0.516	0.363	0.553	0.370	F	F
NGC 4233	1.15	0.277	0.162	G	0.578	0.401	0.564	0.390	F	F
NGC 4249	1.32	0.048	0.040	G	0.204	0.142	0.194	0.127	F	F
NGC 4251	0.79	0.508	0.387	G	0.637	0.503	0.584	0.466	F	F
NGC 4255	1.34	0.434	0.127	S	0.622	0.374	0.606	0.370	F	F
NGC 4259	1.93	0.553	0.450	G	0.231	0.081	0.237	0.068	F	S
NGC 4261	0.44	0.222	0.222	G	0.090	0.090	0.085	0.085	S	S
NGC 4262	1.39	0.117	0.117	C	0.297	0.254	0.309	0.250	F	F
NGC 4264	1.26	0.191	0.191	C	0.541	0.355	0.499	0.341	F	F
NGC 4267	0.53	0.079	0.079	C	0.260	0.241	0.282	0.253	F	F
NGC 4268	0.93	0.552	0.348	G	0.491	0.333	0.492	0.330	F	F
NGC 4270	0.96	0.543	0.424	G	0.378	0.289	0.406	0.294	F	F
NGC 4278	0.72	0.103	0.134	G	0.201	0.208	0.178	0.203	F	F
NGC 4281	0.69	0.535	0.502	G	0.757	0.702	0.651	0.621	F	F
NGC 4283	1.44	0.033	0.031	G	0.172	0.155	0.171	0.151	F	F
NGC 4324	0.83	0.434	0.197	G	0.639	0.407	0.592	0.389	F	F
NGC 4339	0.55	0.060	0.060	G	0.311	0.302	0.325	0.312	F	F
NGC 4340	0.62	0.227	0.237	G	0.499	0.481	0.458	0.442	F	F
NGC 4342	2.45	0.442	0.263	S	0.537	0.307	0.528	0.306	F	F

Table B1 – *continued*

Name	R_{\max}	ϵ_e	$\epsilon_{e/2}$	Band (ϵ)	V/σ_e	$V/\sigma_{e/2}$	λ_{Re}	$\lambda_{Re/2}$	F/S (R_e)	F/S ($R_e/2$)
(1)	(2)	(3)	(4)	(5)	(6)	(7)	(8)	(9)	(10)	(11)
NGC 4346	0.77	0.533	0.360	G	0.571	0.428	0.576	0.439	F	F
NGC 4350	0.77	0.674	0.550	G	0.658	0.460	0.638	0.480	F	F
NGC 4365	0.33	0.254	0.254	G	0.114	0.114	0.088	0.088	S	S
NGC 4371	0.51	0.309	0.313	G	0.541	0.541	0.482	0.482	F	F
NGC 4374	0.44	0.147	0.147	G	0.026	0.026	0.024	0.024	S	S
NGC 4377	1.30	0.157	0.228	S	0.443	0.314	0.473	0.338	F	F
NGC 4379	0.90	0.224	0.258	G	0.386	0.294	0.398	0.300	F	F
NGC 4382	0.34	0.202	0.202	G	0.174	0.174	0.163	0.163	F	F
NGC 4387	1.10	0.373	0.351	G	0.391	0.315	0.399	0.317	F	F
NGC 4406	0.24	0.211	0.211	G	0.090	0.090	0.052	0.052	S	S
NGC 4417	0.89	0.566	0.418	G	0.542	0.395	0.548	0.392	F	F
NGC 4425	0.62	0.676	0.587	G	0.438	0.363	0.454	0.384	F	F
NGC 4429	0.48	0.402	0.402	G	0.455	0.455	0.396	0.396	F	F
NGC 4434	1.15	0.058	0.082	G	0.249	0.186	0.288	0.199	F	F
NGC 4435	0.52	0.468	0.465	G	0.672	0.667	0.599	0.597	F	F
NGC 4442	0.62	0.335	0.307	G	0.350	0.329	0.363	0.338	F	F
NGC 4452	0.42	0.880	0.880	G	0.765	0.765	0.648	0.648	F	F
NGC 4458	0.68	0.121	0.119	G	0.150	0.161	0.072	0.079	S	S
NGC 4459	0.64	0.148	0.128	G	0.477	0.450	0.438	0.408	F	F
NGC 4461	0.68	0.392	0.306	G	0.486	0.405	0.511	0.430	F	F
NGC 4472	0.26	0.172	0.172	G	0.073	0.073	0.077	0.077	S	S
NGC 4473	0.71	0.421	0.396	G	0.255	0.263	0.229	0.250	F	F
NGC 4474	0.72	0.570	0.468	G	0.439	0.347	0.446	0.353	F	F
NGC 4476	1.07	0.353	0.375	G	0.236	0.298	0.153	0.266	S	F
NGC 4477	0.44	0.135	0.135	C	0.216	0.216	0.221	0.221	F	F
NGC 4478	0.98	0.165	0.175	G	0.221	0.175	0.233	0.177	F	F
NGC 4483	1.02	0.346	0.251	G	0.474	0.271	0.465	0.273	F	F
NGC 4486	0.28	0.037	0.037	G	0.024	0.024	0.021	0.021	S	S
NGC 4486A	1.96	0.224	0.224	G	0.379	0.379	0.351	0.351	F	F
NGC 4489	0.62	0.085	0.075	G	0.176	0.125	0.168	0.117	F	F
NGC 4494	0.48	0.173	0.173	G	0.219	0.219	0.212	0.212	F	F
NGC 4503	0.61	0.446	0.429	G	0.510	0.451	0.523	0.470	F	F
NGC 4521	0.89	0.566	0.482	G	0.794	0.566	0.682	0.534	F	F
NGC 4526	0.45	0.361	0.361	G	0.563	0.563	0.453	0.453	F	F
NGC 4528	1.15	0.392	0.129	G	0.112	0.116	0.096	0.102	S	F
NGC 4546	0.66	0.527	0.465	G	0.653	0.572	0.639	0.579	F	F
NGC 4550	0.88	0.649	0.633	G	0.122	0.072	0.105	0.061	S	S
NGC 4551	0.92	0.284	0.259	G	0.311	0.285	0.295	0.259	F	F
NGC 4552	0.46	0.047	0.047	G	0.051	0.051	0.049	0.049	S	S
NGC 4564	0.78	0.560	0.477	G	0.640	0.532	0.619	0.536	F	F
NGC 4570	0.70	0.626	0.551	G	0.586	0.470	0.603	0.498	F	F
NGC 4578	0.70	0.289	0.282	G	0.669	0.596	0.596	0.544	F	F
NGC 4596	0.56	0.254	0.254	C	0.310	0.297	0.297	0.280	F	F
NGC 4608	0.56	0.115	0.115	C	0.194	0.180	0.203	0.185	F	F
NGC 4612	0.75	0.204	0.196	R	0.428	0.345	0.407	0.324	F	F
NGC 4621	0.50	0.365	0.364	G	0.273	0.272	0.291	0.291	F	F
NGC 4623	0.64	0.673	0.648	G	0.660	0.602	0.598	0.564	F	F
NGC 4624	0.42	0.065	0.065	C	0.292	0.288	0.297	0.293	F	F
NGC 4636	0.25	0.094	0.094	G	0.039	0.039	0.036	0.036	S	S
NGC 4638	0.87	0.606	0.657	G	0.909	0.895	0.691	0.715	F	F
NGC 4643	0.61	0.249	0.199	G	0.321	0.323	0.255	0.254	F	F
NGC 4649	0.35	0.156	0.156	G	0.123	0.123	0.127	0.127	F	F
NGC 4660	1.39	0.441	0.315	G	0.603	0.518	0.553	0.475	F	F
NGC 4684	0.70	0.598	0.596	G	0.713	0.665	0.622	0.600	F	F
NGC 4690	0.96	0.266	0.257	G	0.149	0.130	0.151	0.123	S	S
NGC 4694	0.52	0.547	0.546	G	0.275	0.276	0.289	0.295	F	F
NGC 4697	0.37	0.447	0.447	G	0.363	0.363	0.322	0.322	F	F
NGC 4710	0.74	0.699	0.395	G	0.731	0.496	0.652	0.456	F	F
NGC 4733	0.74	0.060	0.060	C	0.096	0.088	0.086	0.076	F	F
NGC 4753	0.49	0.213	0.213	G	0.537	0.537	0.467	0.467	F	F
NGC 4754	0.68	0.480	0.480	C	0.445	0.395	0.467	0.418	F	F

Table B1 – continued

Name	R_{\max}	ϵ_e	$\epsilon_e/2$	Band (ϵ)	V/σ_e	$V/\sigma_e/2$	λ_{Re}	$\lambda_{Re}/2$	F/S (R_e)	F/S ($R_e/2$)
(1)	(2)	(3)	(4)	(5)	(6)	(7)	(8)	(9)	(10)	(11)
NGC 4762	0.40	0.852	0.852	G	0.783	0.783	0.724	0.724	F	F
NGC 4803	2.02	0.282	0.266	S	0.192	0.063	0.181	0.054	F	S
NGC 5103	1.47	0.594	0.400	G	0.588	0.370	0.573	0.386	F	F
NGC 5173	1.71	0.133	0.124	G	0.164	0.110	0.168	0.106	F	F
NGC 5198	0.62	0.146	0.151	G	0.074	0.072	0.061	0.057	S	S
NGC 5273	0.61	0.108	0.116	G	0.554	0.512	0.517	0.482	F	F
NGC 5308	0.78	0.735	0.637	G	0.641	0.478	0.651	0.510	F	F
NGC 5322	0.56	0.307	0.304	G	0.126	0.121	0.073	0.067	S	S
NGC 5342	1.51	0.586	0.425	G	0.637	0.410	0.626	0.439	F	F
NGC 5353	0.77	0.552	0.541	G	0.689	0.544	0.618	0.532	F	F
NGC 5355	1.59	0.296	0.263	G	0.288	0.214	0.286	0.211	F	F
NGC 5358	1.32	0.592	0.395	G	0.675	0.461	0.610	0.442	F	F
NGC 5379	0.67	0.627	0.696	G	0.920	0.794	0.719	0.677	F	F
NGC 5422	0.68	0.604	0.537	G	0.588	0.475	0.600	0.501	F	F
NGC 5473	0.71	0.211	0.211	C	0.437	0.326	0.447	0.324	F	F
NGC 5475	0.86	0.697	0.568	G	0.965	0.711	0.759	0.638	F	F
NGC 5481	0.79	0.214	0.161	G	0.159	0.165	0.103	0.091	S	S
NGC 5485	0.61	0.171	0.208	G	0.176	0.160	0.165	0.149	F	F
NGC 5493	1.08	0.561	0.640	G	1.095	1.089	0.740	0.773	F	F
NGC 5500	1.10	0.234	0.214	G	0.178	0.155	0.172	0.146	F	F
NGC 5507	1.36	0.252	0.144	G	0.479	0.302	0.495	0.306	F	F
NGC 5557	0.60	0.169	0.157	G	0.048	0.044	0.049	0.045	S	S
NGC 5574	1.04	0.627	0.566	G	0.443	0.371	0.452	0.382	F	F
NGC 5576	0.76	0.306	0.310	G	0.097	0.088	0.102	0.091	S	S
NGC 5582	0.63	0.320	0.321	G	0.676	0.668	0.564	0.567	F	F
NGC 5611	1.57	0.559	0.485	G	0.816	0.661	0.691	0.590	F	F
NGC 5631	0.81	0.127	0.167	G	0.171	0.193	0.110	0.166	S	F
NGC 5638	0.61	0.091	0.079	G	0.253	0.222	0.265	0.229	F	F
NGC 5687	0.76	0.379	0.349	G	0.486	0.440	0.479	0.435	F	F
NGC 5770	0.99	0.061	0.061	C	0.242	0.171	0.273	0.174	F	F
NGC 5813	0.38	0.170	0.170	G	0.161	0.161	0.071	0.071	S	S
NGC 5831	0.81	0.136	0.203	G	0.088	0.093	0.063	0.065	S	S
NGC 5838	0.67	0.361	0.297	G	0.521	0.464	0.521	0.460	F	F
NGC 5839	1.03	0.100	0.169	G	0.385	0.269	0.430	0.298	F	F
NGC 5845	2.57	0.264	0.236	G	0.402	0.368	0.404	0.358	F	F
NGC 5846	0.38	0.062	0.062	R	0.037	0.037	0.032	0.032	S	S
NGC 5854	0.79	0.575	0.426	G	0.761	0.531	0.678	0.515	F	F
NGC 5864	0.59	0.695	0.658	G	0.630	0.556	0.603	0.550	F	F
NGC 5866	0.44	0.566	0.566	G	0.349	0.349	0.319	0.319	F	F
NGC 5869	0.85	0.245	0.244	G	0.433	0.387	0.428	0.383	F	F
NGC 6010	0.84	0.742	0.539	G	0.703	0.555	0.679	0.556	F	F
NGC 6014	0.58	0.419	0.434	G	0.418	0.378	0.387	0.353	F	F
NGC 6017	2.53	0.455	0.405	G	0.441	0.352	0.429	0.340	F	F
NGC 6149	1.65	0.325	0.279	G	0.656	0.579	0.563	0.513	F	F
NGC 6278	1.02	0.409	0.401	G	0.521	0.368	0.576	0.411	F	F
NGC 6547	1.22	0.674	0.456	G	0.616	0.410	0.632	0.444	F	F
NGC 6548	0.66	0.107	0.107	C	0.315	0.254	0.326	0.261	F	F
NGC 6703	0.68	0.019	0.017	G	0.043	0.038	0.041	0.035	S	F
NGC 6798	0.95	0.461	0.372	G	0.488	0.322	0.483	0.310	F	F
NGC 7280	0.82	0.363	0.377	G	0.606	0.538	0.557	0.503	F	F
NGC 7332	0.85	0.674	0.469	G	0.490	0.291	0.561	0.338	F	F
NGC 7454	0.65	0.364	0.363	R	0.106	0.091	0.094	0.067	S	S
NGC 7457	0.62	0.470	0.438	G	0.546	0.478	0.519	0.465	F	F
NGC 7465	2.17	0.364	0.406	G	0.343	0.352	0.283	0.294	F	F
NGC 7693	1.34	0.233	0.275	G	0.686	0.440	0.616	0.408	F	F
NGC 7710	1.84	0.581	0.548	S	0.293	0.136	0.340	0.137	F	S
PGC016060	1.32	0.694	0.681	G	1.019	0.682	0.759	0.616	F	F
PGC028887	1.49	0.323	0.312	G	0.282	0.332	0.145	0.252	S	F
PGC029321	2.32	0.140	0.146	G	0.339	0.187	0.336	0.175	F	F
PGC035754	2.60	0.275	0.333	G	0.258	0.275	0.210	0.266	F	F
PGC042549	1.57	0.369	0.450	G	0.771	0.560	0.673	0.529	F	F

Table B1 – *continued*

Name	R_{\max}	ϵ_e	$\epsilon_{e/2}$	Band (ϵ)	V/σ_e	$V/\sigma_{e/2}$	λ_{Re}	$\lambda_{Re/2}$	F/S (R_e)	F/S ($R_e/2$)
(1)	(2)	(3)	(4)	(5)	(6)	(7)	(8)	(9)	(10)	(11)
PGC044433	3.00	0.335	0.184	S	0.362	0.205	0.357	0.200	F	F
PGC050395	1.58	0.233	0.240	G	0.149	0.111	0.138	0.089	S	S
PGC051753	1.54	0.549	0.538	G	0.668	0.538	0.587	0.513	F	F
PGC054452	1.17	0.189	0.175	G	0.435	0.316	0.416	0.307	F	F
PGC056772	1.87	0.493	0.467	G	0.386	0.443	0.310	0.420	F	F
PGC058114	1.95	0.185	0.213	R	0.228	0.159	0.176	0.132	F	F
PGC061468	1.58	0.231	0.230	G	0.464	0.391	0.409	0.360	F	F
PGC071531	2.35	0.305	0.235	R	0.323	0.263	0.333	0.266	F	F
PGC170172	2.08	0.195	0.372	G	0.287	0.192	0.324	0.218	F	F
UGC03960	0.93	0.190	0.081	G	0.130	0.109	0.119	0.094	S	F
UGC04551	1.59	0.137	0.137	G	0.252	0.205	0.277	0.214	F	F
UGC05408	2.68	0.168	0.248	G	0.290	0.270	0.278	0.292	F	F
UGC06062	1.55	0.449	0.449	C	0.472	0.325	0.475	0.332	F	F
UGC06176	1.58	0.252	0.330	G	0.670	0.447	0.585	0.426	F	F
UGC08876	1.93	0.408	0.180	S	0.311	0.182	0.341	0.189	F	F
UGC09519	2.48	0.484	0.407	G	0.764	0.631	0.632	0.552	F	F

Note. Column (1): galaxy name from the principal designation from the LEDA; column (2): largest equivalent aperture radius reached by the SAURON maps in units of R_e ; columns (3) and (4): moment ellipticity measured within one effective radius R_e and one-half effective radius $R_e/2$, these being replaced by the global ellipticity measured from the outer isophotes for galaxies with clear bars (see text) as indicated by a ‘C’ in column (5) of this table; column (5): ‘Band’ refers to the source of the radial ellipticity profiles, with G, R and S referring to the green, red and SAURON photometry, and ‘C’ for galaxies which have strong bars significantly affecting the measurement of ϵ_e , and for which the outer ellipticity measurement ϵ_{glob} (see Paper II) is used instead; columns (6) and (7): V/σ as measured within $1R_e$ and $R_e/2$; columns (8) and (9): λ_R measured within $1R_e$ and $R_e/2$; and columns (10) and (11): FR (F) or SR (S) according to the λ_R and ϵ values at R_e and $R_e/2$. Table (B1) is also available at our project website: <http://purl.org/atlas3d>

It is worth mentioning the effect on the inclination for both V/σ and λ_R values. As shown by Binney (2005), for an inclination i , we have ($i = 90^\circ$ being edge-on):

$$(V/\sigma)(i) = C(i)(V/\sigma)_{\text{edge-on}}$$

with $C(i) = \sin i / \sqrt{1 - \beta \cos^2 i}$ where we assumed an axisymmetric system for which the intersection between the velocity ellipsoid and a plane perpendicular to the axis of symmetry is a circle everywhere. Assuming relation B1 holds, this translates into

$$\lambda_R(i) = C(i) \frac{\lambda_{\text{Redge-on}}}{\sqrt{1 + [C^2(i) - 1]\lambda_{\text{Redge-on}}^2}}.$$

We finally include in Fig. B5 a Monte Carlo simulation as in Fig. 15 (see Section 5.1), but here for a smaller aperture of $R_e/2$ for

comparison. We use a distribution for the intrinsic ellipticities ϵ_{intr} of the simulated sample with two Gaussians: one centred at $\epsilon_0 = 0.7$ with a width $\sigma_\epsilon = 0.2$ as for the simulation at $1R_e$ and the other component centred at $\epsilon_0 = 0.6$, representing 30 per cent of the one at $\epsilon_0 = 0.7$. This second Gaussian is required to account for the fact that for an aperture of $R_e/2$ the intrinsic ellipticity distribution is offset to values slightly smaller than for an aperture size of R_e ; the larger one better probes the outer more flattened component of (most) FRs. We again fix the anisotropy distribution also as a Gaussian with a mean of $m_\beta = 0.5$ and a dispersion of $\sigma_\beta = 0.1$, truncated at $0.8\epsilon_{\text{intr}}$.

This paper has been typeset from a \LaTeX file prepared by the author.